High-resolution estimates of Southwest Indian Ridge plate motions, 20 Ma to present

C. DeMets,[1] S. Merkouriev[2,3] and D. Sauter[4]

[1]*Department of Geoscience, University of Wisconsin-Madison, Madison, WI 53706, USA. E-mail:* chuck@geology.wisc.edu
[2]*Pushkov Institute of Terrestrial Magnetism of the Russian Academy of Sciences, St Petersburg Filial. 1 Mendeleevskaya Liniya, St Petersburg 199034, Russia*
[3]*Saint Petersburg State University, Institute of Earth Sciences Universitetskaya nab., 7-9, St. Petersburg 199034, Russia*
[4]*Ecole et Institut de Physique du Globe, CNRS-UMR 7516 5 rue Descartes Strasbourg cedex, France*

SUMMARY

We present the first estimates of Southwest Indian Ridge (SWIR) plate motions at high temporal resolution during the Quaternary and Neogene based on nearly 5000 crossings of 21 magnetic reversals out to C6no (19.72 Ma) and the digitized traces of 17 fracture zones and transform faults. Our reconstructions of this slow-spreading mid-ocean ridge reveal several unexpected results with notable implications for regional and global plate reconstructions since 20 Ma. Extrapolations of seafloor opening distances to zero-age seafloor based on reconstructions of reversals C1n (0.78 Ma) through C3n.4 (5.2 Ma) reveal evidence for surprisingly large outward displacement of 5 ± 1 km west of 32°E, where motion between the Nubia and Antarctic plates occurs, but 2 ± 1 km east of 32°E, more typical of most mid-ocean ridges. Newly estimated SWIR seafloor spreading rates are up to 15 per cent slower everywhere along the ridge than previous estimates. Reconstructions of the numerous observations for times back to 11 Ma confirm the existence of the hypothesized Lwandle plate at high confidence level and indicate that the Lwandle plate's western and eastern boundaries respectively intersect the ridge near the Andrew Bain transform fault complex at 32°E and between ∼45°E and 52°E, in accord with previous results. The Nubia–Antarctic, Lwandle–Antarctic and Somalia–Antarctic rotation sequences that best fit many magnetic reversal, fracture zone and transform fault crossings define previously unknown changes in the Neogene motions of all three plate pairs, consisting of ∼20 per cent slowdowns in their spreading rates at $7.2^{+0.9}_{-1.4}$ Ma if we enforce a simultaneous change in motion everywhere along the SWIR and gradual 3°–7° anticlockwise rotations of the relative slip directions. We apply trans-dimensional Bayesian analysis to our noisy, best-fitting rotation sequences in order to estimate less-noisy rotation sequences suitable for use in future global plate reconstructions and geodynamic studies. Notably, our new Nubia–Antarctic reconstruction of C5n.2 (11.0 Ma) predicts 20 per cent less opening than do two previous estimates, with important implications for motion that is estimated between the Nubia and Somalia plates. A Nubia–Somalia rotation determined from our Nubia–Antarctic and Somalia–Antarctic plate rotations for C5n.2 (11.0 Ma) predicts cumulative opening of 45 ± 4 km (95 per cent uncertainty) across the northernmost East Africa rift since 11.0 Ma, 70 per cent less than a recent 129 ± 62 km opening estimate based on a now-superseded interpretation of Anomaly 5 along the western portion of the SWIR.

Key words: Plate motions; Africa; Antarctica.

1 INTRODUCTION AND BACKGROUND

The Southwest Indian Ridge (SWIR), which extends nearly 8000 km between the Bouvet and Rodriguez triple junctions (Fig. 1), has accommodated separation between Antarctica and Africa since the breakup of Gondwanaland at 160 Ma (Lawver & Scotese 1987). Numerous authors have estimated rotations that reconstruct SWIR

magnetic lineations and fracture zones both as a means of studying this slow spreading centre and to facilitate paleogeographic and kinematic reconstructions of the Atlantic, Pacific and Indian Ocean basins. Reconstructions of the SWIR that were published in the 1970s and 1980s documented its Late Cretaceous and Cenozoic opening histories, but with relatively few details due to the sparse magnetic anomaly and bathymetric data that were then available
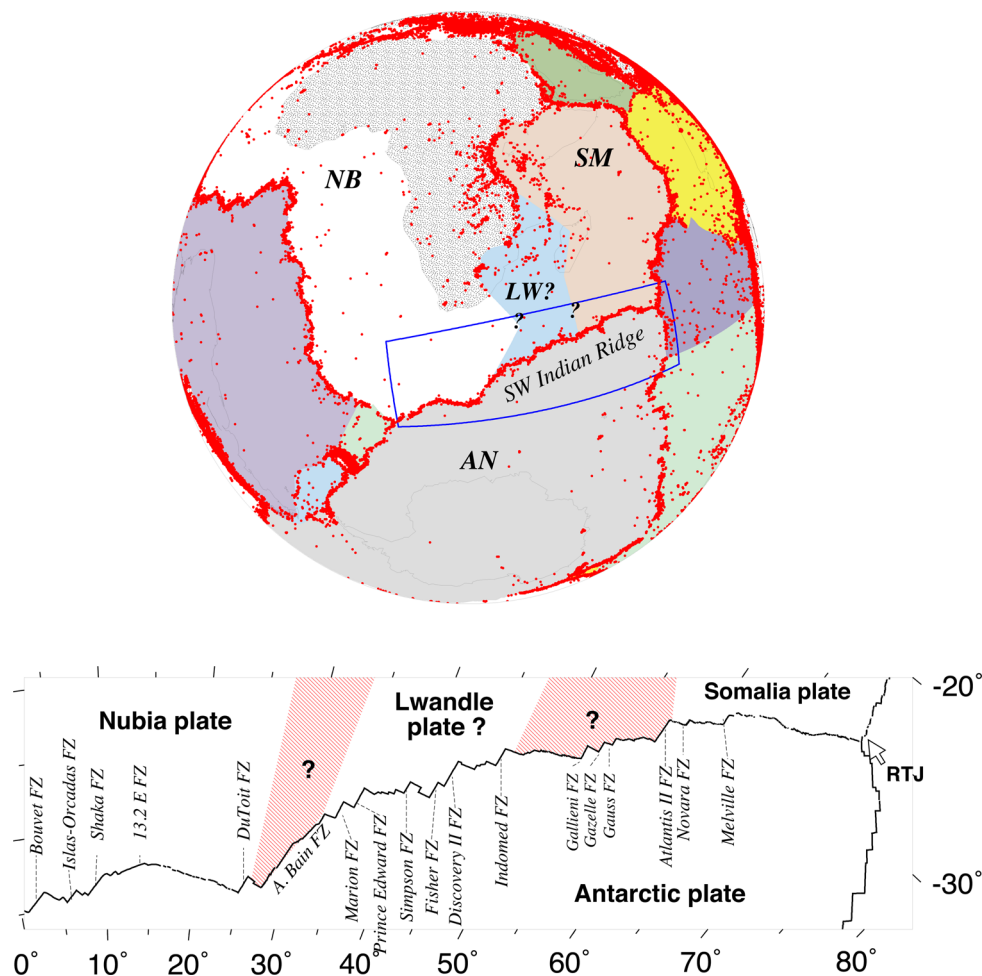
Figure 1. Location map for study area. Upper map shows plate tectonic setting of the study area and earthquakes from 1964 through 2013 shallower than 60 km and with magnitudes over 3.5. Blue rectangle delimits the region shown in the lower map. Lower map is an oblique Mercator projection of the Southwest Indian Ridge with prominent transforms labelled. AN—Antarctic plate; LW—Lwandle plate; NB—Nubia plate; RTJ—Rodrigues triple junction; SM—Somalia plate.

(e.g. Fisher & Sclater 1983; Patriat 1983; Molnar *et al.* 1988). More recent reconstructions, which are based on much improved mapping of SWIR magnetic anomalies, document several significant changes in motion since the Late Cretaceous, including a factor-of-three decrease in seafloor spreading rates and 45° anticlockwise rotation in the plate opening direction between 76 and 70 Ma (Patriat *et al.* 1985; Royer *et al.* 1988; Bernard *et al.* 2005), a 30° clockwise rotation in the plate opening direction between 55 and 50 Ma (Royer *et al.* 1988; Bernard *et al.* 2005; Cande *et al.* 2010) and a 50 per cent slowdown in spreading rates at ≃24 Ma (Patriat *et al.* 2008).

Studies of SWIR plate motion during the Quaternary and Neogene periods (23 Ma to present) must cope with several challenges, including sparse data coverage in some areas, highly oblique spreading across some ridge segments, poorly expressed magnetic anomalies due to the slow-to-ultraslow SWIR spreading rates and uncertainties about the present configuration of plate boundaries north of the SWIR due to the ongoing breakup of the Africa plate into Nubia, Somalia and possibly Lwandle plates. Reflecting these difficulties, early efforts to use plate kinematic data from the SWIR to find the southern termination of the East Africa rift system and estimate an angular velocity to describe Nubia–Somalia plate motion were unsuccessful (Chase 1972; Minster *et al.* 1974; Chase 1978; Minster & Jordan 1978; DeMets *et al.* 1990; Jestin *et al.* 1994). Using 3-Ma-average SWIR seafloor spreading rates and transform

fault directions, Chu & Gordon (1999) were the first to detect (at statistically significant levels) the intersection of a diffuse Nubia–Somalia plate boundary with the SWIR (near 35°E) and estimate a Nubia–Somalia plate angular velocity that correctly predicted slow divergence in eastern Africa. From an expanded set of SWIR plate motion data, Horner-Johnson *et al.* (2005) estimated refined limits of 26°–32°E for the intersection of the Nubia–Somalia boundary with the SWIR and Horner-Johnson *et al.* (2007) reported the first kinematic evidence for an additional Lwandle plate sandwiched between the Nubia and Somalia plates (Fig. 1).

Herein, we describe a new high-resolution model for Quaternary and Neogene plate motion across the SWIR, consisting of best-fitting and noise-reduced rotations that reconstruct SWIR opening at 21 different times since 20 Ma. Although other authors have reconstructed in detail the spreading histories of geographically limited areas along the ridge (e.g. Dick *et al.* 1991; Hosford *et al.* 2003; Baines *et al.* 2007) or have estimated plate motion everywhere along the ridge since 3.2 Ma (Horner-Johnson *et al.* 2005, 2007) or 11 Ma (Lemaux *et al.* 2002; Royer *et al.* 2006), this is the first study to document in detail the post-20-Ma spreading history of the entire SWIR. The paper is organized as follows: After brief descriptions of the data and methods that we employ, we derive the first estimates of outward displacement along the SWIR from inversions of geographic clusters of young magnetic anomaly
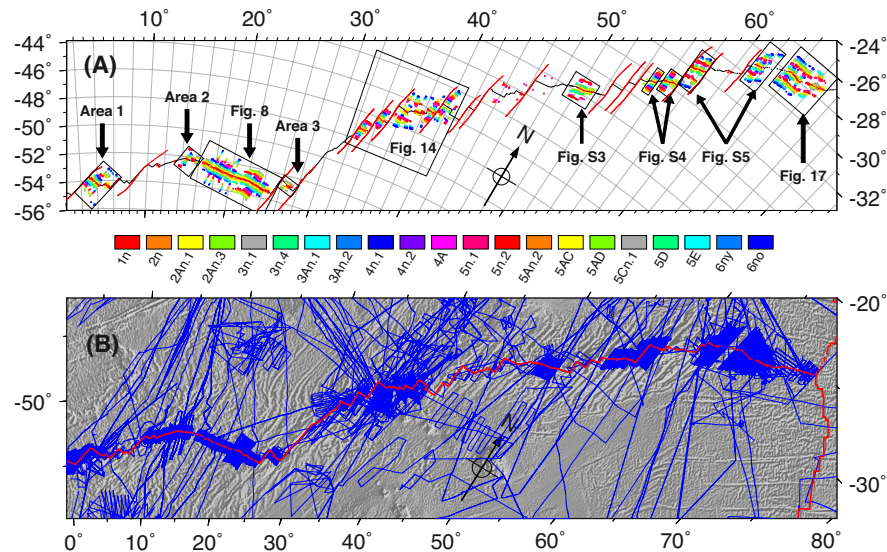
Figure 2. (A) Crossings of magnetic reversals C1n through C6no and fracture zones (red circles) used to estimate the best-fitting sequences of plate rotations described in the text. Reconstructions of magnetic reversal crossings in Areas 1–3 are shown in Fig. 9. (B) Tracks of shipboard and airborne magnetic data compiled for the analysis. Plate boundary is marked by the red line. Map shows a 1-km bathymetric grid extracted from ETOPO1 (www.ngdc.noaa.gov/global/relief/ETOPO1). Both maps are oblique Mercator projections.

crossings from densely surveyed areas of the ridge. We then examine the kinematic evidence for the existence of a Lwandle plate (Fig. 1) and the location of its boundaries where they intersect the SWIR (Horner-Johnson *et al.* 2007) using our numerous data for all times back to 11.0 Ma. Based on the values for outward displacement and plate geometries estimated in the previous stages of the analysis, we then solve for time sequences of best-fitting and noise-reduced rotations for the Nubia–Antarctic, Lwandle–Antarctic and Somalia–Antarctic plate pairs and use stage rotations determined from both sets of finite rotations to document the kinematic evolution for each plate pair since 20 Ma.

2 DATA

The data we use to estimate SWIR rotations consist of magnetic anomaly identifications along the numerous track lines compiled for this analysis (Fig. 2), and fracture zone flow lines and transform faults digitized from bathymetry. Each is described briefly below.

2.1 Magnetic reversal crossings

The magnetic data compiled for the analysis are from American, French, Italian, Japanese and South African cruises (Fig. 2B). They include data from seven detailed surveys focused mostly on seafloor younger than 10 Ma and data from numerous isolated or transit tracks (Fig. 2B). The former are critical for identifying the full sequence of magnetic reversals that is necessary for constructing a chronologically detailed plate motion model, and the latter contribute important information in areas where dense survey data are not available. Of particular note, this is the first kinematic study to estimate Somalia–Antarctic rotations with data from the dense, well-navigated R/V *Marion Dufresne* 135 multibeam and magnetic survey between 60.5°E and 67°E (Cannat *et al.* 2006; Sauter *et al.* 2008). Other dense surveys used for the analysis include an Italian–Russian survey near the Bouvet triple junction (2°–5°E) (Ligi *et al.* 1999), near-ridge surveys from 9°15′E to 16°E (Dick *et al.* 2003)

and 15°E to 35°E (Grindlay *et al.* 1998; Sclater *et al.* 2005), the Agulhaus 4401 survey from ≈22°–24°E, French surveys from 49°15′E to 57°E (Patriat *et al.* 1997), and American and Japanese surveys from 55°E to 58.5°E (Dick *et al.* 1991; Hosford *et al.* 2003).

From these data, we identified crossings of 21 magnetic polarity reversals (Table 1 and Figs 2 and 3), coinciding with either the young or old edge of a magnetic polarity interval (Fig. 3). The reversals range in age from 0.781 Ma (the old edge of Anomaly 1n) to 19.72 Ma (the old edge of Anomaly 6) and are the same as those used to document Quaternary and Neogene motions along other plate boundaries (DeMets *et al.* 2005; Merkouriev & DeMets 2006, 2008, 2014a,b). Reversal ages (Table 1) are adopted from the GTS12 astronomically tuned geomagnetic reversal time scale (Hilgen *et al.* 2012; Ogg 2012).

Our initial expectations for extracting closely spaced reversal identifications from the SWIR magnetic anomalies were low due to the limited fidelity of the magnetic anomalies that are typically created by slow- to ultraslow spreading centres. At such slow spreading rates, magnetic anomalies that are associated with short-duration magnetic polarity chrons (such as Anomaly 2, which had a duration of 0.17 Mr) are often unrecognizable in a surface magnetic profile or may only be an inflection in adjacent magnetic anomalies associated with longer-duration polarity intervals. We identified reversals via a careful comparison of each observed profile to a synthetic profile that was created at an appropriate spreading rate (typically 14 mm yr^{-1}) and with an appropriate anomaly phase shift. Anomalies C5AC and C5AD were particularly difficult to distinguish from the other reversals within the 5AA-5B anomaly sequence. The greater noise associated with identifying their precise locations results in greater scatter for reconstructions and stage rotations for times and intervals before C5An.2 (12.5 Ma).

Of the ∼7000 reversal crossings that we identified from the data, we discarded or revised a higher percentage (≈30 per cent) of our initial reversal identifications than was the case for our studies of faster spreading centres, where the rejection rate was only 5–10 per cent (e.g. Merkouriev & DeMets 2006, 2008, 2014a,b). The higher degree of inconsistency in our reversal identifications for

Table 1. Data summary.

Magnetic reversal	Age (Ma)	Nubia–Antarctic[a] # data : wrms (km)		Lwandle–Antarctic[a] # data : wrms (km)		Somalia–Antarctic[a] # data : wrms (km)	
		Anom	FZ	Anom	FZ	Anom	FZ
1no	0.781	250 : 1.87	57 : 0.49	128 : 1.35	48 : 0.31	207 : 1.34	46 : 0.14
2ny	1.778	181 : 1.41	63 : 0.59	102 : 1.40	51 : 0.66	143 : 1.03	58 : 0.47
2An.1y	2.581	195 : 1.51	46 : 0.70	105 : 1.58	59 : 1.01	185 : 1.06	33 : 0.92
2An.3o	3.596	152 : 1.54	60 : 1.10	83 : 1.15	52 : 1.03	138 : 1.34	53 : 1.07
3n.1y	4.187	125 : 1.61	44 : 1.30	61 : 1.30	35 : 1.11	102 : 1.71	33 : 1.41
3n.4o	5.235	117 : 1.74	57 : 1.24	59 : 1.32	61 : 1.27	83 : 1.67	55 : 1.58
3An.1y	6.033	104 : 1.47	43 : 1.09	47 : 1.24	60 : 1.27	69 : 1.41	38 : 1.87
3An.2o	6.733	90 : 1.37	47 : 1.03	47 : 1.41	47 : 1.62	53 : 1.47	37 : 1.49
4n.1y	7.528	78 : 1.60	52 : 1.04	27 : 1.43	36 : 2.05	45 : 0.90	51 : 1.55
4n.2o	8.108	53 : 1.24	29 : 1.28	28 : 2.15	46 : 2.49	53 : 1.07	35 : 1.57
4Ao	9.105	33 : 2.19	83 : 1.40	80 : 1.44	66 : 2.55	108 : 1.44	68 : 2.03
5n.1y	9.786	47 : 2.40	61 : 1.65	100 : 2.00	56 : 3.02	141 : 1.59	45 : 1.69
5n.2o	11.056	54 : 1.85	75 : 2.00	106 : 1.69	77 : 3.33	147 : 1.30	85 : 2.21
5An.2o	12.474	36 : 2.26	74 : 1.44	30 : 1.92	85 : 3.83	84 : 1.94	85 : 2.61
5ACy	13.739	41 : 1.85	77 : 1.10	26 : 1.69	109 : 4.26	74 : 1.83	85 : 3.06
5ADo	14.609	40 : 1.94	37 : 1.28	17 : 2.36	73 : 4.17	63 : 1.84	53 : 3.57
5Cn.1y	15.974	18 : 2.00	80 : 1.37	9 : 1.00	35 : 3.95	60 : 2.05	109 : 3.87
5Dy	17.235	0 : 0.00	0 : 0.00	17 : 1.11	108 : 4.14	39 : 2.15	72 : 3.98
5Ey	18.056	0 : 0.00	0 : 0.00	38 : 1.37	75 : 4.00	60 : 1.81	63 : 3.89
6ny	18.748	17 : 1.93	170 : 2.24	40 : 1.63	35 : 4.13	71 : 2.48	56 : 4.25
6no	19.722	14 : 2.22	194 : 2.65	40 : 2.81	40 : 4.22	62 : 2.19	236 : 4.75

[a]The rotations for C1n are also constrained by transform fault crossings, as follows: 580 crossings for Nubia–Antarctica with a wrms misfit of 0.92 km; 657 crossings for Lwandle–Antarctica with a wrms misfit of 1.23 km; 397 crossings for Somalia–Antarctica with a wrms misfit of 1.03 km. Chron designators followed by a 'y' or 'o' respectively indicate the young or old edge of the chron. The ages for all the reversals are from the astronomically tuned time scale of Ogg (2012) (also see Hilgen *et al.* 2012). Anom and FZ respectively indicate the number of magnetic anomaly and fracture zone crossings that were used to estimate the finite rotations in Tables 2–4. Ages estimated for the fracture zone crossings are approximated based on their position along their respective flow lines, but are not used for the inversion. Instead, each fracture zone crossing contributes information to the finite rotation estimates for all ages. wrms is the weighted root-mean-square misfit in km of a best-fitting rotation adjusted for the number of parameters that were estimated to fit the data.

the SWIR is not surprising. Schouten & Denham (1979) compare ideal, synthetic magnetic anomaly profiles determined from known sequences of magnetic reversals to magnetic profiles they generated while applying basic statistical assumptions about the processes that create new seafloor (such as assuming that dyke injection occurs as a Gaussian process centred on the spreading axis). They show that the agreement between the former and latter magnetic profiles becomes increasingly worse at progressively slower spreading rates. Higher rates of false reversal identifications are thus implied for slow spreading rates.

Although we were concerned that discarding a significant fraction of the data might bias our results or skew the statistics of our rotation misfits and hence bias the rotation uncertainties, the 4822 reversal crossings that we retained to estimate the SWIR plate rotations are numerous and well distributed along the ridge (Fig. 2A). In particular, the rotations that reconstruct reversals younger than ~11 Ma should be robust with respect to any remaining problems with our reversal identifications because those rotations are estimated from numerous reversal crossings from five or more spreading segments well distributed along the ridge. The rotations for reversals older than 11 Ma are, to varying degrees, less robust because they are sometimes based on fewer data (Table 1) that are more poorly distributed along the plate boundary. At the extreme, we were unable to identify enough crossings of C5D or C5E west of the Bain transform fault to estimate Nubia–Antarctic rotations for either of those times.

We assigned uncertainties of ±1.4–1.6 km to the individual reversal crossings based on an analysis of their dispersions relative to their reconstructed best-fitting great-circle segments.

Further details are given in Section S2 of the supplementary document.

2.2 Fracture zone flow lines and transform faults

From multibeam, single-beam and altimetrically derived bathymetry available through the Marine Geoscience Data System (www.geomapapp.org and Carbotte *et al.* 2004), we digitized 18 transform faults and 17 fracture zones to constrain present and paleo-slip directions along the SWIR (displayed by red lines in Fig. 2A). Fracture zone crossings were digitized every ~0.5 km for areas of the bathymetric grid that are constrained by multibeam data and every ~2.0 km for areas of the grid constructed from single-beam data or satellite altimetry.

Uncertainties were assigned to each transform fault and fracture zone crossing as follows: If we found morphologic features within a fracture zone or transform fault valley that clearly bound the zone of present-day or past faulting, we used the cross-valley distance between those features to assign an uncertainty for the fracture zone or transform fault trace at that location. If no such features were apparent, we estimated the uncertainty from the width of the fracture zone or transform fault valley. Valley widths varied from 3 km where multibeam or single-beam bathymetry clearly delineate the zone of present or past faulting to 20 km where faulting is constrained only to lie somewhere within the fracture zone valley. We equated the half-width of the fracture zone valley to the 95 per cent uncertainty in the location of the shear zone within the valley and the 1-σ uncertainty to half of the 95 per cent uncertainty. This resulted in
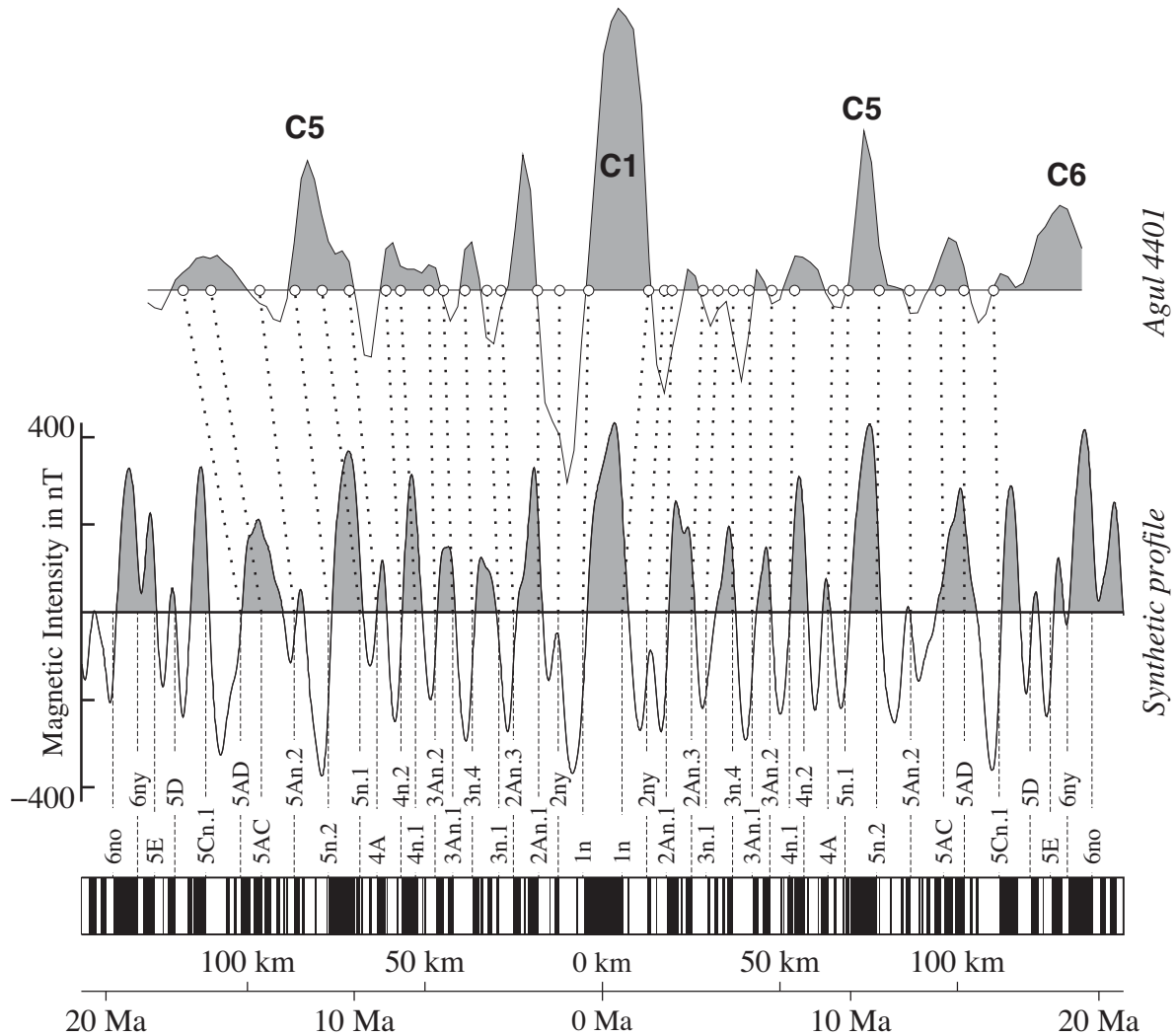
Figure 3. Comparison of magnetic anomaly profile from the Agulhaus 4401 survey of the Southwest Indian Ridge, 21°E to 24°E, to a synthetic magnetic profile created using a 14 mm yr^{-1} spreading rate, a ridge azimuth of N75°W, a 500-m wide reversal transition zone, and ambient and paleomagnetic inclinations and declinations appropriate for the survey area. The magnetic block model and magnetic reversal correlation points (dotted lines) used for this study are shown below the synthetic magnetic anomaly profile.

1-σ uncertainties of ± 0.8 km to ± 5 km for all of the transform fault and fracture zone crossings.

3 METHODS

3.1 Best-fitting rotations, uncertainties and stage rotations

Best-fitting finite rotations are estimated directly from the observations via an inversion that optimizes the weighted least-squares fits of reconstructed magnetic reversal, fracture zone and transform fault crossings. Further details about the fitting functions for each type of observation are found in Section S1 of the supplementary document and Merkouriev & DeMets (2014a,b). The best-fitting rotation sequence for a single plate pair is estimated via a simultaneous inversion of all of the data, including the crossings of all 21 magnetic reversals included in the study and all of the fracture zone and transform fault crossings for that plate pair. A simultaneous inversion of the data is required so that all of the rotation parameters can adjust in order to optimize the fit to the fracture zone flow lines.

All of the finite rotations are corrected during the inversion for the influence of outward displacement.

Most of the rotation uncertainties are estimated with a segment-based bootstrapping method (Merkouriev & DeMets 2006 and Section S1). The bootstrapped uncertainties for 56 of the 61 estimated rotations are larger than are uncertainties estimated from the geometric distribution of the observations (Chang 1988; Kirkwood *et al.* 1999). For the five rotations with geometrically derived covariances that are larger than their bootstrapped covariances, we adopted the more conservative geometrically derived covariances. Further details are given in Section S1.

Following Royer & Chang (1991), we use $\hat{\kappa} = (N - m)/\chi^2$ to quantify the dispersion of the observations with respect to the predictions of our best-fitting rotations, where N is the number of observations, m the number of parameters used to fit the data and χ^2 the weighted least-squares misfit to the data.

We describe the evolution of SWIR motion using stage rotations and uncertainties that are derived rigorously from the finite rotations and their uncertainties. To keep the 2-σ (95 per cent) uncertainties in the estimated stage rates below ± 1 mm yr^{-1}, we estimate

interval rates from stage rotations that span periods of 1 to 3 Myr. Intervals this long reduce the influence of reversal age uncertainties to only ± 0.1 mm yr^{-1} assuming likely errors of ± 5000–10 000 yr in astronomically calibrated reversal ages (Lourens *et al.* 2004). Uncertainties in the values for outward displacement that we use to correct the finite rotations add additional uncertainties to the finite rotations, but do not significantly affect the stage rotations because any bias that is introduced into the finite rotations via the correction for outward displacement cancels out upon differencing the finite rotations to estimate stage rotations.

3.2 Noise-reduced rotations and plate motion changes from REDBACK

Noise in rotation sequences with high temporal resolution often gives rise to kinematically and geodynamically implausible changes in plate motion over short time scales (Iaffaldano *et al.* 2012). If a time-progression of rotations is visualized as a series of progressively longer Euler vectors that describe an irregular (noisy) path through 3-space, then a sequence of rotations that describe a simpler (i.e. less noisy) path through 3-space can be selected such that it remains faithful to the original rotation sequence within their 3-D ellipsoidal uncertainties. Iaffaldano *et al.* (2012) describe and implement a trans-dimensional Bayesian method for accomplishing this goal, including the ability to identify whether and when changes in plate motion occur. We apply the newly available REDBACK software (Iaffaldano *et al.* 2014) to the newly estimated best-fitting rotations and their covariances in order to estimate noise-reduced rotations and determine the timing of any changes in SWIR plate motion. In order to remain true to the original observations, we tested the fits of all of the noise-reduced rotations against the original observations to guard against solutions that violate the data constraints. Details are given below.

4 RESULTS

The analysis is presented in four stages. In Section 4.1, we estimate the magnitude of outward displacement from inversions of young magnetic reversal crossings in order to establish the basis for correcting finite rotations that are estimated later in the analysis. In Section 4.2, we test for the existence of the postulated Lwandle plate and search for the locations where its western and eastern boundaries intersect the SWIR using the numerous observations for all times between 0.78 Ma (C1n) and 11.06 Ma (C5n.2). In Sections 4.3–4.5, we determine best-fitting and noise-reduced sequences of plate motion rotations and uncertainties for the Nubia–Antarctic, Lwandle–Antarctic and Somalia–Antarctic plate pairs and evaluate the fits of both to the original observations. The statistics of the reconstruction misfits are provided in Supplementary Section S4 and Fig. S6 for interested readers. In Section 4.6, we use the best-fitting and noise-reduced rotations to describe the Quaternary and Neogene plate motion history of the SWIR and determine when changes in plate motion occurred.

4.1 Evidence for and magnitude of outward displacement

Near-bottom magnetic surveys of magnetic polarity transition zones (Sempere *et al.* 1987) show that the midpoints of magnetic polarity transition zones are shifted outward from their idealized locations by 1 km or more nearly everywhere along the mid-ocean ridges. This outward bias in magnetic reversal locations, hereafter referred to as

outward displacement, results partly from processes such as dyke injection, flow extrusion and normal faulting, which collectively widen magnetic transition zones near or at the ridge axis (Atwater & Mudie 1973; Kidd 1977; Macdonald *et al.* 1983), but may be enhanced by horizontal thermal contraction of young, rapidly cooling seafloor (Kumar & Gordon 2009). Reconstructions of young magnetic reversals along seven globally distributed spreading centres indicate that reversal locations are displaced outward from the axis of seafloor spreading along all seven spreading centres (DeMets & Wilson 2008). Their results indicate that two-sided outward displacement, defined as the net outward displacement of two conjugate magnetic lineations across the ridge, ranges from 1 to 5 km and averages 2 km for the spreading centres sampled in their analysis.

Correcting plate motion estimates for outward displacement is mainly important for studies of recent plate motions, for which outward displacement may constitute a significant fraction of the cumulative plate motion. For example, for a hypothetical spreading centre with two-sided outward displacement of 2 km, spreading rates that are estimated by reconstructing the edges of the Brunhes anomaly (C1n) will overestimate the full, true spreading rate by 2.6 mm yr^{-1} (i.e. 2 km/0.78 Myr) absent any correction for outward displacement. For the SWIR, where recent spreading rates average ~ 15 mm yr^{-1}, the implied bias in seafloor spreading rates averaged over the past 0.78 Ma (C1n) is ~ 20 per cent absent any correction for outward displacement.

To date, no work has been published about magnetic polarity zone transition widths or outward displacement along the SWIR. Below, we use the numerous crossings of reversals C1n through C3n.4 (5.2 Ma) to evaluate the evidence for and estimate the magnitude of outward displacement along the SWIR.

4.1.1 Example of the method

Our method for estimating outward displacement, illustrated in Fig. 4, is based on the simple principle that an extrapolation of reconstructed seafloor opening distances versus seafloor ages back to zero-age seafloor should give a distance-axis intercept of zero if seafloor spreading has been steady and magnetic reversal boundary locations and reversal ages are free from systematic biases. For example, we subdivided 562 crossings of magnetic reversals C1n through C3n.4 located between 16°E and 25°E (Fig. 4A) into eastern and western geographic subsets, inverted the reversal crossings from each area to find the C1n-to-C3n.4 opening angles that best reconstruct the sequence of reversal crossings within each area, converted the opening angles to their equivalent opening distances at the midpoint of their respective survey areas (Fig. 4B) and inverted the opening distances from each area and their associated reversal ages to find a best-fitting opening rate and distance-axis intercept for each area (Fig. 4B).

The age progressions of opening distances in both areas are linear (Fig. 4B), indicating that seafloor spreading rates have remained steady in both areas since 5.2 Ma. The observations thus satisfy a necessary condition for estimating outward displacement via this method. Linear regressions of both age-distance sequences give positive distance-axis intercepts of 5.3 ± 0.4 km and 3.8 ± 0.4 km (Figs 4B and C) and nearly identical, best-fitting opening rates of 13.8 and 14.1 mm yr^{-1} (Fig. 4B). Reversals C1n through C3n.4 are thus shifted outward from their their idealized locations in both areas, consistent with the pattern observed everywhere along the mid-ocean ridge system (DeMets & Wilson 2008).
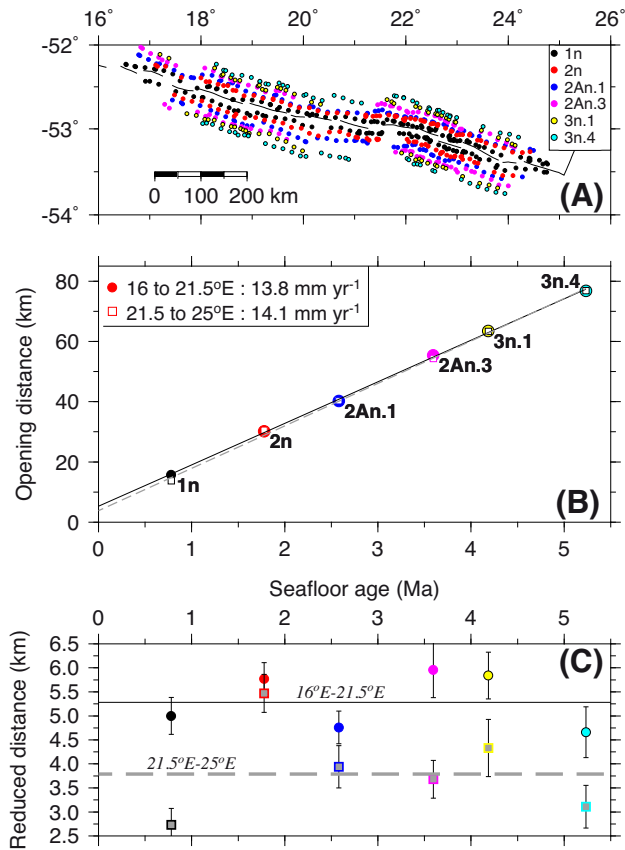
Figure 4. Estimation of outward displacement, 16°E to 25°E. (A) Locations of the magnetic reversal crossings that are used to estimate the C1n-to-C3n.4 opening distances. (B) Opening distances estimated by reconstructing reversal crossings west of ∼21.5°E (circles) and east of ∼21.5°E (squares). Method is described in Section 4.1.1. The opening distances and uncertainties for each area are determined along the centrally located small circles shown by the dashed lines in panel (A). Regressions of the age sequences of opening distances from the two areas give best-fitting slopes for each area (shown by the solid and dashed lines) that differ by only 0.3 mm yr^{-1} or 2 per cent. The positive Y-axis intercepts (3.8 km and 5.3 km) are evidence for outward displacement (see the text). (C) Opening distances and 1-σ uncertainties from panel (B) reduced by their best-fitting slopes (but not by their Y-axis intercepts). The coloured circles show reduced distances for the western area (16°E to 21.5°E). Squares show reduced distances for the eastern area (21.5°E to 25°E).

4.1.2 Variations in outward displacement along the SWIR

We applied the method described above to the entire SWIR by subdividing the SWIR into eleven, non-overlapping areas between the Bouvet and Rodriguez triple junctions (Fig. 5B), each with enough crossings of C1n through C3n.4 to estimate outward displacement for that section of the ridge (Fig. 5B). The values of outward displacement for these eleven areas range from -0.9 ± 0.9 to 6.8 ± 1.2 km (Fig. 5A). Ten of the eleven distance-axis intercepts are positive and the only negative value differs insignificantly from zero. All four outward displacement estimates for ridge segments that are located west of the Bain transform fault are greater than 3.5 km, whereas all seven estimates of outward displacement for areas east of the Bain transform fault are less than 3.5 km (Fig. 5A).

Given that random errors may be responsible for some or possibly all of the scatter in the eleven estimates shown in Fig. 5(A), we tested whether the 11 age–distance sequences are consistent with the simple hypothesis that outward displacement has the same

magnitude everywhere along the SWIR. Separate inversions of the eleven age-distance sequences to determine their best-fitting slopes and distance-axis intercepts (i.e. the results shown in Fig. 5A) gives a summed least-squares misfit of $\chi^2 = 117.3$. A simultaneous inversion of all eleven age-distance sequences to estimate one best-fitting slope per area and one distance-axis intercept for the entire SWIR gives $\chi^2 = 239.0$. The latter, simpler model is rejected at the 99.97 per cent confidence level based on an F-ratio comparison of the two fits. Significant variations in the magnitude of outward displacement thus occur along the ridge.

Guided by the pattern in Fig. 5(A), we repeated the above inversion, but estimated separate values for outward displacement from the observations west and east of the Bain transform fault. This gave respective distance-axis intercepts of 5.0 ± 0.2 km (1-σ) and 1.9 ± 0.3 km (grey bars in Fig. 5A) for the observations west and east of the Bain transform fault. The increase in the least-squares misfit associated with estimating only two, area-averaged distance-axis intercepts instead of separate intercepts for all eleven areas is statistically insignificant (the significance level is less than 20 per cent). The 5.0-km and 1.9-km average intercept values are thus consistent with the underlying dispersion in the observations.

4.1.3 Influence of possible opening rate changes since 5 Ma

We tested the robustness of the above estimates for outward displacement by relaxing the requirement that SWIR spreading rates have remained steady since 5.2 Ma and instead requiring steady spreading rates only since 1.8 Ma. For this case, an inversion of the C1n (0.78 Ma) and C2n (1.78 Ma) opening distances for areas west of the Bain transform fault gives a best distance-axis intercept of 2.5 ± 0.4 km, significantly less than the 5.0 ± 0.2 km estimate based on our inversion of opening distances for C1n through C3n.4. An inversion of the opening distances from east of the Bain transform fault gives a best distance-axis intercept of 1.6 ± 0.6 km, insignificantly different from the 1.9 ± 0.3 km estimate based on the C1n-C3n.4 opening distances.

These results raise the question of whether to calibrate finite rotations for areas west of the Andrew Bain transform fault by 5.0 ± 0.2 km, as suggested by the C1n-C3n.4 opening distances, or 2.5 ± 0.4 km, as indicated by the C1n-C2n distances. We elected to use the 5 km calibration for two reasons. First, the weighted root-mean-square (wrms) misfits to the opening distances that were inverted for the two estimates do not differ significantly. Applying the principle of Occam's Razor, we thus adopt the simpler model as the preferred estimate, namely, the model that enforces constant spreading rates over the past 5.2 Myr. Second, GPS measurements from stations on the Nubia and Antarctic plates predict instantaneous Nubia–Antarctica spreading rates that are consistent with outward displacement of 5.0 ± 0.2 km (DeMets, Calais & Merkouriev, 'Reconciling geodetic and geologic estimates of recent plate motion across the Southwest Indian Ridge', in preparation).

In the ensuing analysis, we correct finite rotations determined from data west of the Bain transform fault for outward displacement of 5.0 km and rotations estimated from data east of the Bain transform fault for outward displacement of 2.0 km.

4.2 Triple junction locations and test for existence of the Lwandle plate

Estimates of rotations that reconstruct the motions of the Nubia, Somalia and possibly Lwandle plates north of the SWIR relative
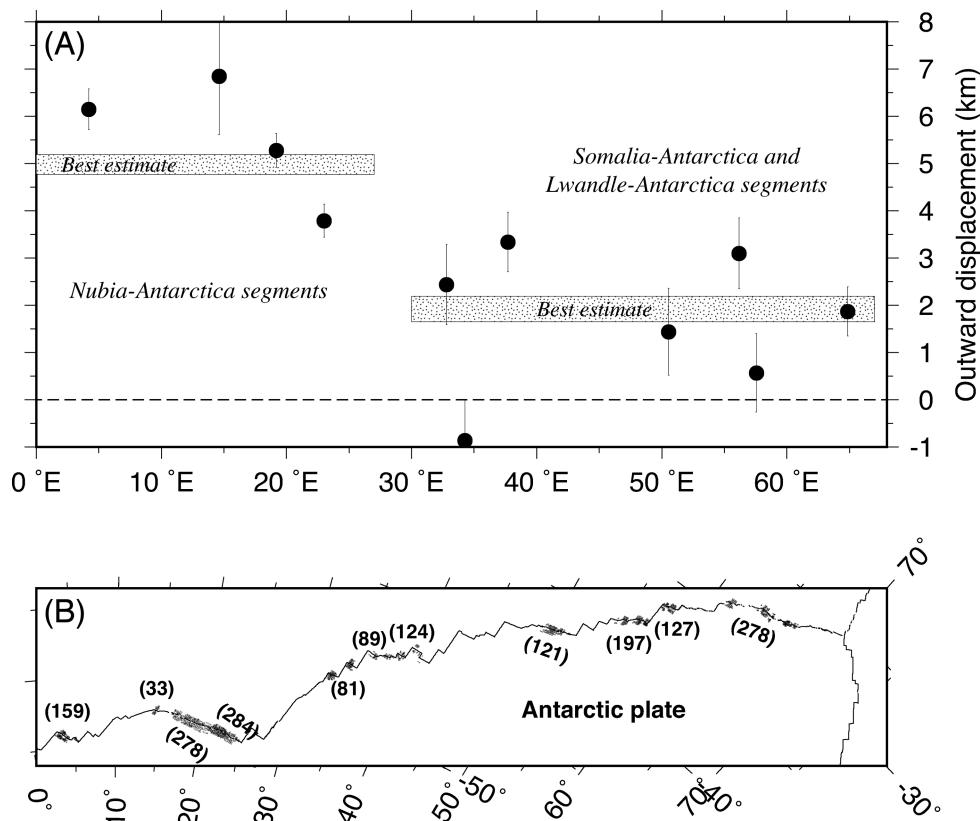
Figure 5. (A) Estimates of SWIR outward displacement from C1n to C3n.4 opening distances derived for the 11 geographic clusters of magnetic reversal crossings shown in panel (B). Each circle shows the *Y*-axis intercept from a linear regression of the reconstructed opening distances and reversal ages for one of the geographic clusters. A simultaneous inversion of all reversal crossings from 0°E to 30°E gives a *y*-axis intercept of 5.0 km (grey bar in panel (A)), representing the best overall estimate of outward displacement for the Nubia–Antarctica plate pair. An inversion of all reversal crossings from 30°E to 70°E gives a best *y*-intercept of 2 km, representing the best outward displacement estimate for the Somalia–Antarctica and Lwandle–Antarctica plate pairs. The scatter of the individual *Y*-axis intercepts (circles) about the average estimates (grey bars) is not statistically significant (see the text). (B) Locations of anomaly crossings used to estimate best opening angles and opening distances at 11 locations along the Southwest Indian Ridge. Numerals within the parentheses give the total anomaly crossings that were used to determine each of the 11 opening distance time series.

to the Antarctic plate require *a priori* information about where the boundaries between the two or three plates north of the SWIR intersect the SWIR. Below, we use our new kinematic data for C1n through C5n.2, consisting of 3996 crossings of 13 distinct magnetic reversals and crossings of the 17 fracture zones and 18 transform faults that are identified in Fig. 2(B), to test for an independent Lwandle plate and define the plate geometries necessary for our analysis. Following brief summaries of results from previous studies of these plate boundaries, which were based on analyses of Chron 2A (3.16 Myr) and C5n.2 (11.06 Ma), we use the Stein & Gordon (1984) method for seeking the best location of a hypothetical plate boundary (suitably modified for this analysis) to seek best locations for boundaries between the Nubia, Somalia and Lwandle plates.

4.2.1 Previous work

From analyses of 3.16-Myr-average spreading rates and transform fault azimuths well-distributed along the SWIR, Horner-Johnson *et al.* (2005) find that the Nubia plate north of the SWIR extends eastward to roughly the Andrew Bain fracture zone at ~26°–32°E. From the same data, Horner-Johnson *et al.* (2007) describe the first plate kinematic evidence for the existence of a Lwandle plate (Fig. 2A), previously postulated by Hartnady (2002), and estimate that its eastern, diffuse boundary with the Somalia plate intersects

the SWIR between the Indomed and Atlantis II fracture zones (47°–57°E). Stamps *et al.* (2008) corroborate the kinematic evidence for a Lwandle plate using a combination of geodetic observations from Africa and nearby islands and kinematic data from Horner-Johnson *et al.* (2007).

Efforts to locate the Nubia–Somalia plate boundary along the SWIR for times before 3 Ma have focused on C5n.2 (11 Ma), with inconsistent results. Lemaux *et al.* (2002) interpret an inconsistency between crossings of C5n.2 that they identified at locations east and west of the Bain transform fault as evidence that the boundary between the two plates intersects the SWIR in the vicinity of the Andrew Bain fracture zone. From their own interpretation of C5n.2 along the SWIR, Patriat *et al.* (2008) however find no evidence for the inconsistency reported by Lemaux *et al.*

4.2.2 Search for the eastern limit of the Nubia plate

Between the Bouvet triple junction (0°E) and Gazelle fracture zone at 53°E, where we focused our search for the eastern boundary of the Nubia plate north of the SWIR, our observations include 2450 crossings of magnetic reversals C1n through C5n.2 and the crossings of 15 transform faults and fracture zones. These greatly exceed the number of data that were used by previous authors for
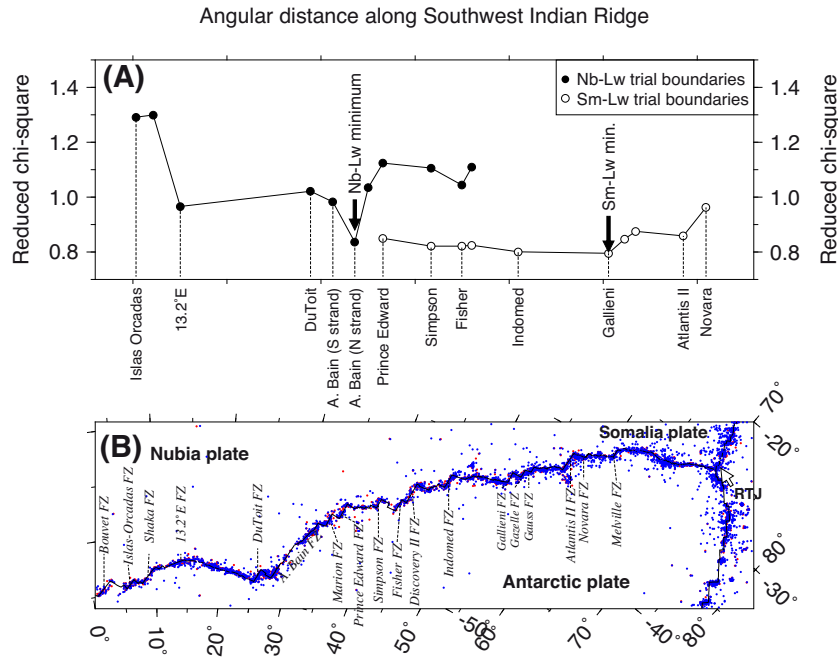
Figure 6. (A) Fits associated with trial locations for the Nubia–Lwandle (filled circle) and Somalia–Lwandle (open circles) plate boundaries where they intersect the Southwest Indian Ridge. Reduced chi-square, the weighted least-squares misfit per degree of freedom, measures the goodness-of-fit associated with each trial boundary, as described in Sections 4.2.2 and 4.2.3. Smaller values correspond to improved fits and are used to identify the optimal locations for the two boundaries. (B) Oblique Mercator map of Southwest Indian Ridge. 'RTJ' is Rodrigues triple junction.

their analyses (Lemaux *et al.* 2002; Horner-Johnson *et al.* 2005, 2007).

For each of eleven, trial intersections of the Nubia plate's eastern boundary with the SWIR (identified by the solid circles in Fig. 6A), we segregated the C1n–C5n.2 data east and west of the assumed boundary and separately inverted the two data subsets to find their respective best-fitting rotation sequences and misfits. The overall misfit associated with a particular trial boundary is equal to the summed least-squares misfits for the two data subsets and is represented by reduced chi-square, the squared misfit per degree of freedom. Variations in the misfits for the 11 trial plate boundaries are used to identify the optimal boundary and evaluate its statistical significance (Stein & Gordon 1984).

The misfits for the 11 trial boundaries vary from 0.84 to 1.30 (solid circles in Fig. 6) and are minimized for a boundary that intersects the SWIR at the northern end of the Bain transform fault. The ~40 per cent improvement in the fit for the best three-plate geometry relative to the fit in which only two plates (Antarctica and Africa) are assumed to meet along the SWIR is significant at confidence levels much greater than 99 per cent. We conclude that the eastern limit of the Nubia plate (i.e. its boundary with the Lwandle plate) intersects the SWIR in the vicinity of the Bain transform fault complex. Boundaries as far west as the DuToit Fracture Zone at 26°E or as far east as the Prince Edward Fracture Zone at 34°E are excluded by the observations. Our result agrees with the boundary location favored by Horner-Johnson *et al.* (2005) based on their analysis of 3.2-Myr-average SWIR seafloor spreading rates.

4.2.3 Lwandle plate and the western limit of the Somalia plate along the SWIR

We used 2447 crossings of C1n through C5n.2 and the digitized traces of 12 transform faults and fracture zones between the Bain transform fault complex and Rodriguez Triple Junction (32°–70°E)

to test for the existence of the Lwandle plate and approximate the Lwandle–Somalia boundary location north of the SWIR. To establish the necessary statistical basis for testing for the existence of an independent Lwandle plate, we inverted all of the SWIR data from 32°–70°E to find C1n-to-C5n.2 best-fitting rotations for an assumed two-plate, Somalia–Antarctic model. This gave $\chi^2 = 4532.1$ for 4607 degrees of freedom, corresponding to reduced chi-square of 0.98.

All twelve of the Lwandle–Somalia trial boundary locations that we tested give rise to fits that improve on that of the two-plate model at significance levels much greater than 99 per cent (open circles in Fig. 6A). The data thus strongly support the existence of an independent Lwandle plate, in accord with results reported by Horner-Johnson *et al.* (2007) and Stamps *et al.* (2008).

The best-fitting model, corresponding to reduced chi-square of 0.80, is associated with a trial boundary at the Gallieni transform fault (52°E). We note however that the data are fit nearly as well for all of the trial boundary locations west of the Gallieni transform fault (open circles in Fig. 6A). As proposed by Horner-Johnson *et al.* (2007), this may indicate that Lwandle–Somalia plate boundary deformation is distributed broadly within the lithosphere east of the Gallieni transform fault, as suggested by diffuse seismicity north of the SWIR between the Gallieni and Indomed fracture zones (47°–52°E in Fig. 6B).

For simplicity, we approximate the Lwandle–Somalia plate boundary as a narrow boundary that intersects the SWIR at 52°E. Although this approximation could, in theory, bias our Lwandle–Antarctic rotation estimates, we note that the wrms misfits of our Lwandle–Antarctic rotations to their underlying plate kinematic data are the same within uncertainties as the wrms misfits for our Nubia–Antarctic and Somalia–Antarctic rotations (Table 1). Any distributed deformation north of the SWIR is thus too slow to degrade the fits to the Lwandle–Antarctic data.

Table 2. Nubia–Antarctic best-fitting finite rotations.

Chron	DOF	Lat.	Long.	Ω	Rotation covariances					
		(°N)	(°E)	(°)	a	b	c	d	e	f
1n	840	−5.46	325.58	−0.112	13.8	−6.5	−6.0	5.4	−0.6	8.6
2n	205	−4.11	326.37	−0.254	61.5	19.8	−94.3	10.2	−24.5	186.3
2An.1	202	−9.88	329.74	−0.372	56.7	15.5	−64.0	14.1	−3.4	136.0
2An.3	183	−13.38	330.36	−0.532	158.1	54.9	−176.3	35.9	−44.6	283.5
3n.1	136	−13.06	331.13	−0.633	199.7	70.8	−235.5	46.1	−51.4	418.6
3n.4	147	−11.11	329.67	−0.753	246.8	76.8	−286.2	44.6	−78.3	443.7
3An.1	120	−7.52	328.04	−0.834	208.6	44.7	−248.7	27.5	−42.9	398.6
3An.2	112	−4.33	326.22	−0.908	296.7	68.3	−360.7	36.3	−81.5	551.2
4n.1	109	−6.74	328.47	−1.046	385.4	100.6	−447.7	62.7	−136.6	645.8
4n.2	65	−5.68	328.17	−1.102	428.7	83.4	−484.2	79.7	−150.1	758.0
4A	103	−8.60	330.57	−1.321	730.0	116.8	−710.5	132.3	−250.9	926.9
5n.1	91	−5.76	329.89	−1.430	922.2	334.1	−942.6	189.9	−406.4	1164.4
5n.2	110	−3.98	328.99	−1.601	264.7	66.5	−301.6	40.1	−88.8	432.8
5An.2	95	−4.57	329.86	−1.807	309.2	85.6	−384.8	64.1	−149.0	571.9
5AC	103	−5.91	330.85	−2.059	257.3	69.3	−252.7	45.6	−92.9	319.6
5AD	64	−6.09	331.58	−2.187	386.5	92.2	−370.0	61.4	−121.5	474.4
5Cn.1	89	−8.52	333.33	−2.500	2369.4	542.5	−2524.0	435.7	−1008.5	3485.1
6ny	178	−5.71	332.63	−2.974	5112.4	373.0	−3135.6	323.2	−358.7	2510.9
6no	199	2.82	326.58	−2.966	726.1	299.4	−438.3	465.3	−149.2	684.0

These finite rotations reconstruct movement of the Nubia plate relative to the Antarctic plate and include corrections for 5 km of outward displacement described in the text. The rotation angles Ω are positive CCW. Each rotation is the mean of 1000 bootstrap solutions (see the text). DOF, the degrees of freedom, equals the total number of anomaly, transform fault and fracture zone flow-line crossings that are used to estimate the rotation for a given time reduced by the number of estimated parameters. The wrms misfits for these rotations are given in Table 1. The Cartesian rotation covariances are calculated in a Nubia–fixed reference frame and have units of 10^{-9} radians^2. Covariances are determined from the bootstrapping procedure described in the text. Elements *a*, *d* and *f* are the variances of the (0°N, 0°E), (0°N, 90°E) and 90°N components of the rotation. The covariance matrices are reconstructed as follows:

$$\begin{pmatrix} a & b & c \\ b & d & e \\ c & e & f \end{pmatrix}.$$

4.3 Nubia–Antarctic plate motion

4.3.1 Best-fitting rotations and poles

The best-fitting sequence of Nubia–Antarctic plate rotations (Table 2) was determined from a simultaneous inversion of 1645 magnetic reversal crossings, 1349 fracture zone crossings and 580 transform fault crossings west of the Bain transform fault. All 19 of the best-fitting rotations are calibrated for 5 km of outward displacement (Section 4.1). The number of reversal crossings that are used to estimate the best-fitting rotations varies by nearly a factor of 20, from as many as 250 for C1n to as few as 14 for C6no (Table 1). Too few crossings of C5D or C5E west of the Bain transform fault were identified to estimate best-fit rotations for either reversal. The kinematic information carried by the 1349 fracture zone crossings is distributed between all 19 best-fitting rotations via the flow-line fitting function for the fracture zone crossings (see also Section S1 in the supplementary documentation). Reconstructions of the data are presented in Section 4.3.3.

The Nubia–Antarctic rotation poles are clustered within several angular degrees of 6°S, 32°W (Fig. 7A), close to the 3.2-Myr-average MORVEL pole for this plate pair (DeMets *et al.* 2010), but ∼10° north of the C5n.2 pole estimated by Royer *et al.* (2006). The irregular path described by the poles and large uncertainties with respect to the distances between the poles suggest that much or possibly all of the scatter in the pole locations is caused by noise. In contrast, the best-fitting rotation angles (Fig. 7C) clearly suggest that the rate of angular rotation has changed during the past 20 Myr. We revisit this topic in more detail in Section 4.6.

4.3.2 Noise-reduced rotations from REDBACK

We applied REDBACK software to the best-fitting rotations and covariances in Table 2 to identify a less noisy rotation sequence that is consistent with the observations. The poles for the noise-reduced rotations (Supporting Information Table S1 and Fig. 7B) are grouped more tightly and describe a smoother path than do the best-fitting poles (Fig. 7B). The noise-reduced rotation angles also change more smoothly than do the best-fitting angles (Fig. 7C). Both sets of angles clearly indicate that at least one significant change in the rate of angular rotation rate has occurred since 20 Ma.

Fits of the best-fitting and noise-reduced rotations to the original data are described next. The kinematic predictions of the newly estimated rotations are presented in Section 4.6 as part of a broader description of the Quaternary and Neogene kinematics of the SWIR.

4.3.3 Magnetic reversal reconstructions and wrms misfits

Figs 8 and 9 show the best-fitting reconstructions of all 1645 Nubia–Antarctica reversal crossings. Our new Nubia–Antarctic rotation estimates are anchored by the numerous identifications of chrons 1n to 5n.2 in the well-surveyed region from 16°E to 25°E (Fig. 8). The magnetic anomaly sequence in much of this region is well defined and the magnetic lineations can be reconstructed with confidence due to the relatively uncomplicated ridge geometry. On the more sparsely surveyed seafloor older than ∼11 Ma, we were only able to identify relatively few crossings of chrons 5Cn.1 (4), 6ny (6) and 6no (7) and no crossings of chrons 5D or 5E. This lack of redundancy increases the possibility that some of these reversal identifications are incorrect.
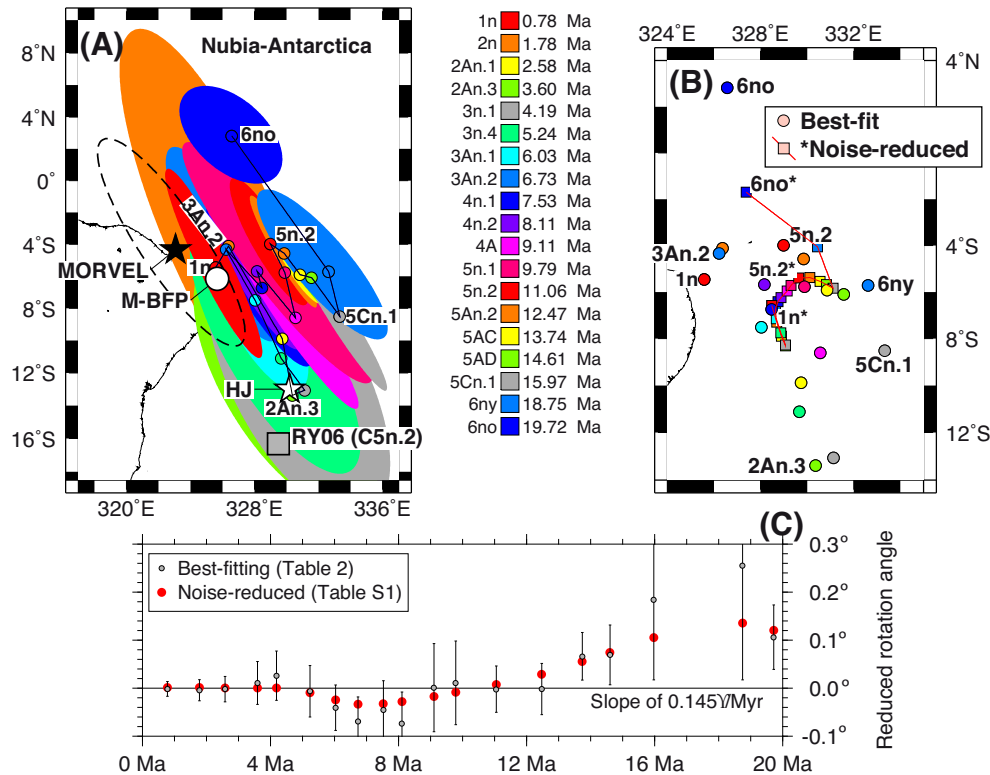
Figure 7. Nubia–Antarctic finite rotation poles (A,B) and angles (C). Panel (A) shows best-fitting poles with 2-D 95 per cent confidence regions (Table 2). The star and dashed ellipse show the location and 95 per cent confidence ellipse of the closure-enforced, 3-Myr-average MORVEL Nubia–Antarctica pole (DeMets *et al.* 2010). Open circle labelled 'M-BFP' is the pole that best fits the MORVEL Nubia–Antarctic data independent of circuit closure constraints. The open star labelled 'HJ' shows the location of the Nubia–Antarctica 3-Myr-average pole from Horner-Johnson *et al.* (2005). The open square labelled 'RY06' shows the corrected C5n.2 pole of Royer *et al.* (2006), whose location is misstated in their fig. 2 caption as 6.32°S, 30.51°W instead of the correct location of 16.32°S, 30.51°W. Panels (B) and (C) compare the Nubia–Antarctic best-fitting finite opening poles and angles from Table 2 to noise-reduced poles and angles from Supporting Information Table S1. Selected anomalies are labelled to facilitate the comparison. The rotation angles are reduced by a slope of 0.145° Myr^{-1} to facilitate the comparison.

Within Area 1 near the Bouvet triple junction (Fig. 9), the opening history for the past 5–10 Myr is constrained by numerous reversal crossings, mostly from seafloor younger than C5n.2 (11 Ma). Identifying the reversal sequence from the low-fidelity magnetic anomalies that flank the ultraslow spreading segments at the west end of the SWIR was challenging, particularly for the most sparsely surveyed seafloor older than ~11 Ma. In particular, we are concerned about the reliability of our identifications of C6no on the Antarctic side of the SWIR, where only two isolated survey tracks may cross Anomaly 6. We are also concerned whether we have correctly identified the paleo-ridge geometry for C6n - if not, then the crossings of Chron 6 south and north of the SWIR may be incorrectly matched. Improved survey coverage of seafloor older than ~10 Ma is clearly needed along the western end of the SWIR.

The wrms misfit of the 19 Nubia–Antarctic best-fitting rotations to the 1645 reversal crossings is 1.67 km, close to the average dispersion for those crossings (Supporting Information Fig. S1). Reconstructing the data with the noise-reduced rotations from Supporting Information Table S1 only increases the wrms misfit by 0.13 km relative to the fits of the best-fitting rotations. We consider this small increase in misfit to be a good trade-off for the less-noisy sequence of rotations that are produced by REDBACK.

4.3.4 Transform fault small-circle fits

All six transform faults that constrain the best-fitting rotation sequence are well fit by small circles around the C1n opening pole (Fig. 10 and Supporting Information Fig. S2). The wrms misfit to the 580 transform fault crossings is 920 m, ~40 per cent smaller than the uncertainties that we assigned to the digitized transform fault crossings. Differences between the digitized transform fault traces and their predicted small-circle traces (Fig. 11) are caused partly by random noise that is introduced during the digitizing process, but may also include misidentifications of the strand(s) of the transform fault that have accommodated most of the plate slip during the past 0.78 Ma. Our newly estimated opening pole for C1n differs insignificantly from the MORVEL Nubia–Antarctic pole (Fig. 7), which is determined partly from the azimuths of four of these six transform faults.

The wrms misfit of the noise-reduced pole for C1n to the six transform fault traces is 1.7 km, larger than for the best-fitting pole (0.9 km). The difference in the location of the noise-reduced pole for C1n relative to the best-fitting pole corresponds to a 2° clockwise rotation in the direction of the predicted, present-day motion at most locations along the plate boundary. We suspect that these small differences indicate that the noise-reduction algorithm functions sub-optimally at the ends of the rotation sequence.
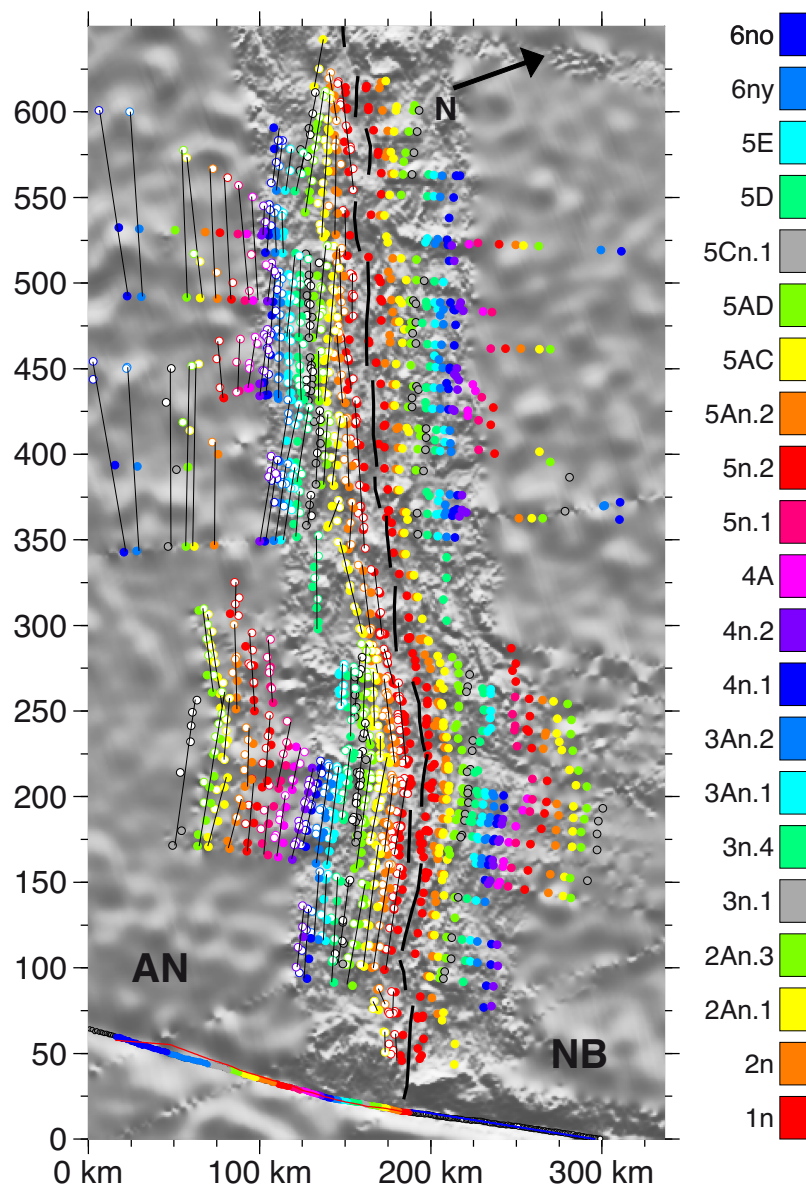
Figure 8. Best-fitting reconstructions of Nubia–Antarctic magnetic lineations. Solid circles show unrotated magnetic reversal crossings identified from shipboard and airborne data (also shown in Fig. 2A). Open circles show reversal crossings on Nubia (NB) plate rotated onto the Antarctic (AN) plate. Black lines show great circle segments that best fit the reconstructed reversal crossings, which define each paleospreading segment. Bold line shows the present plate boundary. See Fig. 2 for the map location. The map is an oblique Mercator projection about a pole located 90° from the centre of the map along a great circle that parallels the ridge trend.

4.3.5 Reconstructed fracture zone flow lines

Seven large-offset and small-offset fracture zones offset the SWIR west of and including the Andrew Bain transform fault. Preliminary inversions that included the traces of all seven consistently gave poor fits to the traces of the Islas Orcadas fracture zone, the short-offset 13°E fracture zone and the Shaka fracture zone north of the SWIR. In contrast, the other four fracture zones and the Shaka fracture zone south of the SWIR were well fit. The poor fits persisted as we experimented with different subsets of the seven fracture zones. We thus elected to exclude the Islas Orcadas, 13°E, and northern Shaka fracture zones and use only the internally consistent traces of the remaining fracture zones to estimate the Nubia–Antarctica rotation sequence.

Fig. 10 and Supporting Information Fig. S2 overlay synthetic flow lines for each fracture zone that we generated with the new Nubia–Antarctica stage rotations on bathymetric maps of all seven fracture zones. The traces of the Bouvet, DuToit and Andrew Bain fracture zones, and the Shaka fracture zone south of the SWIR are geometrically consistent, are well fit by their respective flow lines (Figs 10 and 12) and constitute an internally consistent basis for constraining the Nubia–Antarctica rotations.

In contrast to the good fits described above, the flow lines predicted by the new rotations for the 13°E and Islas Orcadas fracture zones and the Shaka fracture north of the SWIR do not fit the traces we digitized from their bathymetry (Supporting Information Fig. S2). The poor fit to the Islas Orcadas fracture zone may indicate that our interpretation of the fracture zone location is wrong, which
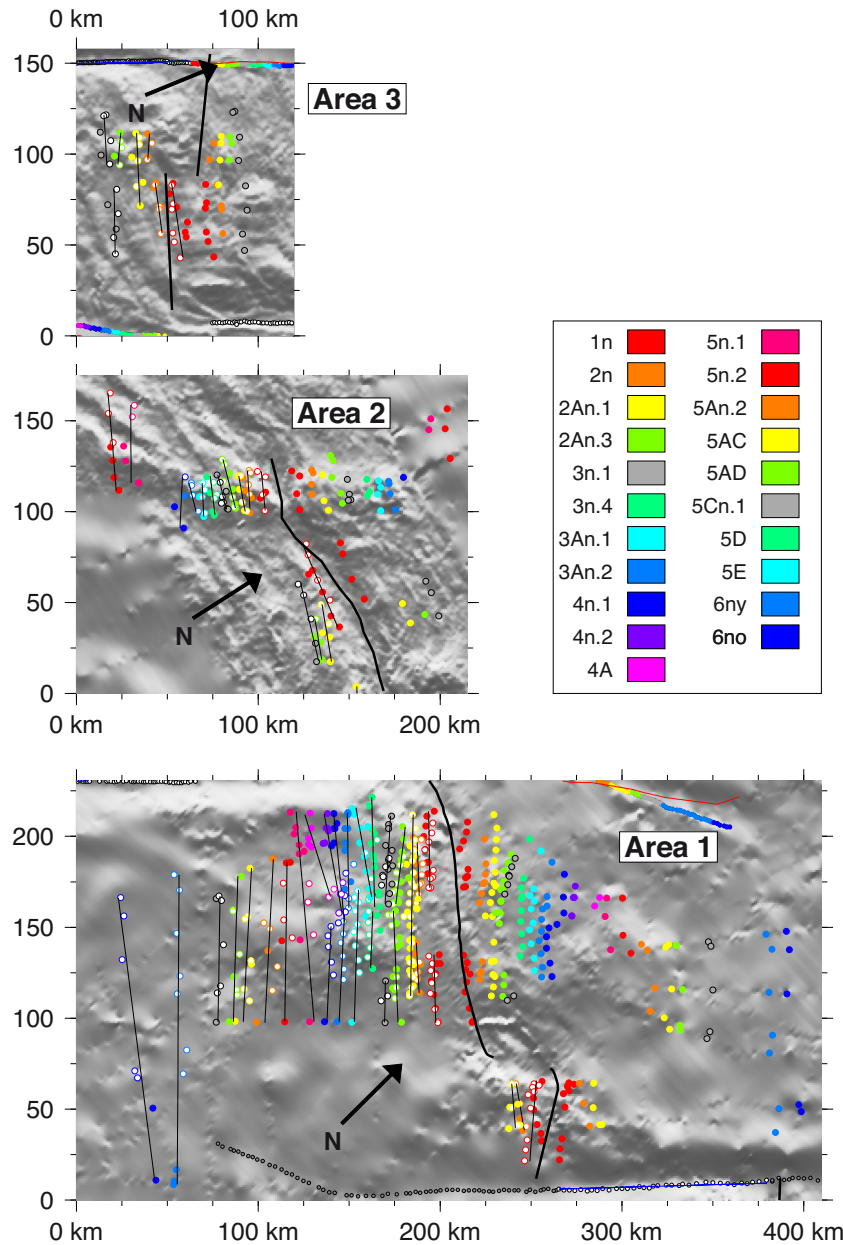
Figure 9. Best-fitting reconstructions of Nubia–Antarctic magnetic lineations from Areas 1–3 located in Fig. 2(A). Solid circles show unrotated magnetic reversal crossings identified from shipboard and airborne data (also shown in Fig. 2A). Open circles show Nubia plate reversal crossings rotated onto the Antarctic plate. Black lines show the great circle segments that best fit the reconstructed reversal crossings. The bold line shows the present plate boundary. All three maps are oblique Mercator projections about the best-fit pole for C4n.1. This and subsequent figures with bathymetry use Version 15.1 of 1-min seafloor bathymetry unless otherwise noted (Sandwell & Smith 1997 and topex.ucsd.edu/marine_topo).

is possible given the absence of detailed bathymetry along the fracture zone valley. Other factors such as one or more ridge jumps may have substantially modified the paleo-ridge and hence fracture zone geometry. The poor fit to the trace of the Shaka fracture zone north of the SWIR (Supporting Information Fig. S2), much of which we digitized from multibeam data, is difficult to explain. More complete multibeam mapping of the seafloor fabric on this end of the SWIR may be required to better understand how the plate boundary and its transform fault offsets evolved to their present configuration.

For the 1349 crossings of the Bouvet, Shaka, DuToit and Bain fracture zones that constrain the Nubia–Antarctica rotation sequence, $\hat{\kappa}$ is 1.31. This indicates that the average misfit is

$\approx$13 per cent smaller than the average uncertainty assigned to each fracture zone crossing (i.e. $1/\sqrt{1.31}$). We take this as evidence that the uncertainties we estimate for the fracture zone crossings are approximately correct. The wrms misfits for the fracture zone crossings increase gradually from 0.5 km for the youngest portions of the fracture zone/flow line to 2.6 km for the older portions (Table 1).

We also used the noise-reduced Nubia–Antarctica stage angular velocities output by the REDBACK software (Supporting Information Table S4) to predict a flow line for each Nubia–Antarctica fracture zone (aquamarine lines in Fig. 10 and Supporting Information Fig. S2). Encouragingly, the noise-reduced flow lines are located within the bounds permitted by the bathymetry and are
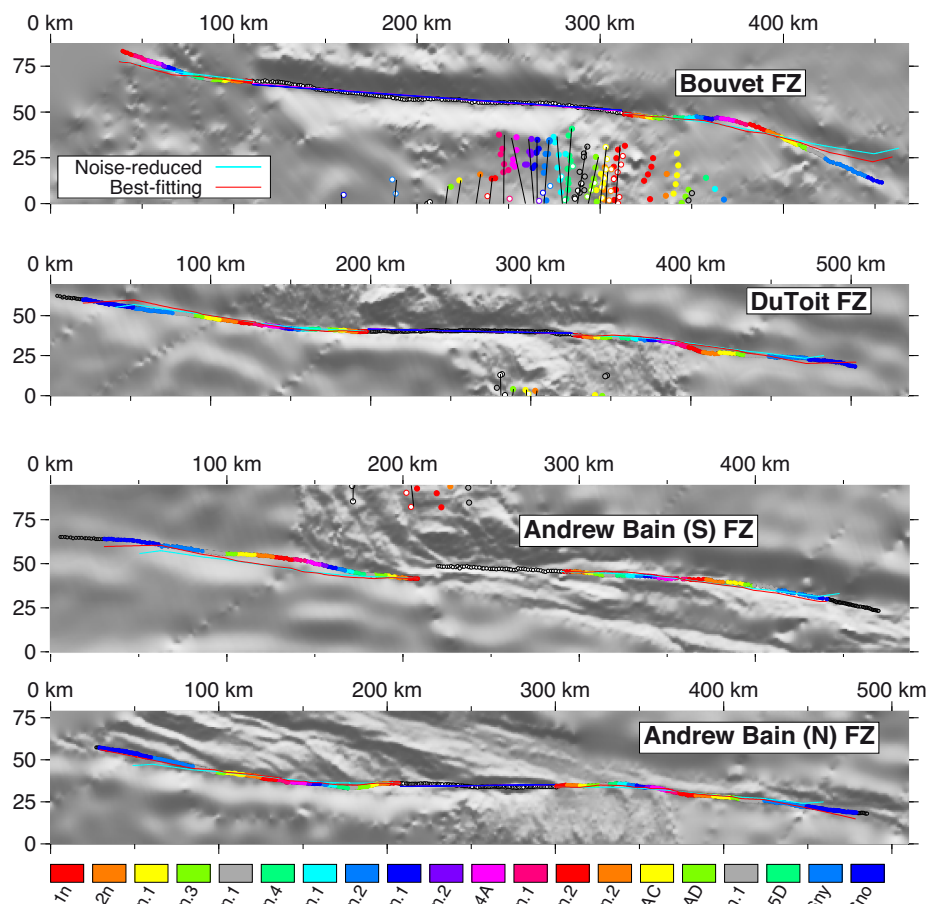
Figure 10. Digitized traces and modelled flow lines for selected Nubia–Antarctica fracture zones and transform faults. All coloured circles identify fracture zone crossings used to constrain the Nubia–Antarctica rotations. Open circles identify transform fault crossings that constrain the C1n rotation. The red and aquamarine flow lines are predicted by stage rotations derived from the best-fitting rotations in Table 2 and the noise-reduced stage angular velocities in Supporting Information Table S4. Blue lines show small-circle fits for the youngest (C1n) opening pole to the actively slipping, transform fault segment of each flow line. Maps are oblique Mercator projections about the Nubia–Antarctica opening pole for C5n.2 (Table 2).

located close to the best-fitting flow lines (red lines in Fig. 10 and Supporting Information Fig. S2). The noise-reduced rotations thus predict a smoother and hence more physically plausible evolution of Nubia–Antarctic slip directions since 20 Ma without violating the underlying bathymetric observations.

4.4 Lwandle–Antarctic plate motion

4.4.1 Best-fitting rotations

Best-fitting Lwandle–Antarctic rotations (Table 3) were determined from a simultaneous inversion of 1190 magnetic reversal crossings, 1254 crossings of six fracture zones and 657 crossings of six transform faults (Table 1), all located between the northern Bain transform fault and the Gallieni transform fault (52°E). All 21 rotations are calibrated for 2 km of outward displacement (Fig. 5).

The newly estimated Lwandle–Antarctic poles are clustered within several angular degrees of 10°N, 39°W (Fig. 13A). The poles migrate slowly southward through time and predict a progressive, anticlockwise change in the plate slip direction. The progression of best-fitting angles is relatively well behaved for C1n to C5n.2 (Fig. 13C), but is noisy for reversals older than C5n.2, most likely due to the sparse and lower-quality survey coverage of seafloor older

than ~11 Ma along the central third of the SWIR. We defer a more detailed description of the evolution of seafloor spreading rates and directions for this plate pair until Section 4.6.

4.4.2 Noise-reduced rotations from REDBACK

Noise-reduced finite rotations for the Lwandle–Antarctic plate pair are given in Supporting Information Table S2 and are illustrated in Fig. 13(B). As expected, the noise-reduced poles are grouped more tightly and describe a smoother path than do the best-fitting poles (Fig. 13B). The noise-reduced angles also exhibit less scatter than do their best-fitting counterparts (Fig. 13C). The fits of the best-fitting and noise-reduced rotations to the original kinematic data are compared below.

4.4.3 Magnetic reversal reconstructions

Nearly all of the magnetic reversal crossings that constrain the Lwandle–Antarctic rotations are from two regions (Fig. 2A), one centred on several well-surveyed spreading segments between the Bain transform fault and 41°E (Fig. 14) and the other limited to 49°–51°E (Supporting Information Fig. S3), where a dense, well-
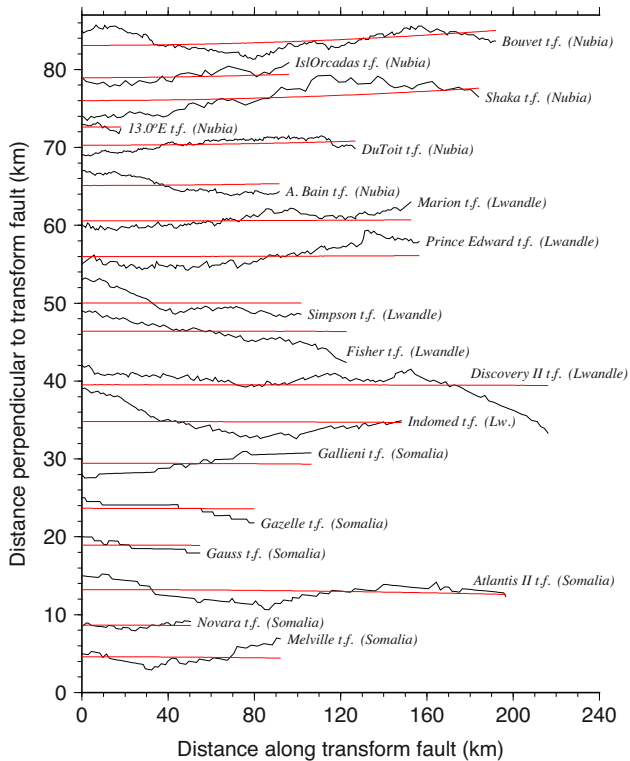
Figure 11. Summary of observed (black) and predicted (red) transform fault traces from Figs 10, 15 and 18, and Supporting Information Fig. S2. Red lines are small circle traces predicted by the C1n rotation poles for the Antarctic plate relative to the Somalia, Lwandle and Nubia plates. Horizontal and vertical axes respectively show the linear distance along each transform fault measured from its southern end and the linear distance orthogonal to each transform fault. The distances displayed on the vertical axis are exaggerated by a factor of four relative to distances shown on the horizontal axis in order to emphasize the misfits and noise in the digitized fault representations.

navigated French survey mapped the seafloor out to ages of ≈12 Ma (Sauter *et al.* 2001). Chrons 1n through 5n.2 are well mapped in both areas and strongly constrain Lwandle–Antarctic plate motions since 11.06 Ma.

Shipboard and aeromagnetic coverage of Lwandle–Antarctic seafloor older than 11 Ma is limited to several spreading segments between the Prince Edward and Simpson transform faults and one segment immediately east of the Simpson transform fault (Fig. 14). Most of the survey tracks in those areas are from South African cruises from the 1970s. Most of the survey tracks from these cruises are oblique to the plate opening direction (Fig. 2B), which complicates their interpretation. In addition, the navigational uncertainties for these older cruises are larger than for modern GPS-navigated cruises and the analog records from those cruises were digitized at sampling rates barely sufficient to define some of the shorter-duration reversals that are used for our analysis. For these reasons, our reversal identifications and interpretation of the paleo-ridge segmentation from 35°E to 41°E are less reliable than for other parts of the SWIR and give rise to more noise in the Lwandle–Antarctic kinematic results than is the case for the Nubia–Antarctic and Somalia–Antarctic plate pairs.

The wrms misfit of the best-fitting rotations to the 1190 Lwandle–Antarctic magnetic reversal crossings is 1.55 km, comparable to that for the other two plate pairs. The noise-reduced rotations increase the wrms misfit to 1.74 km. We consider this difference between the misfits too small to be significant.
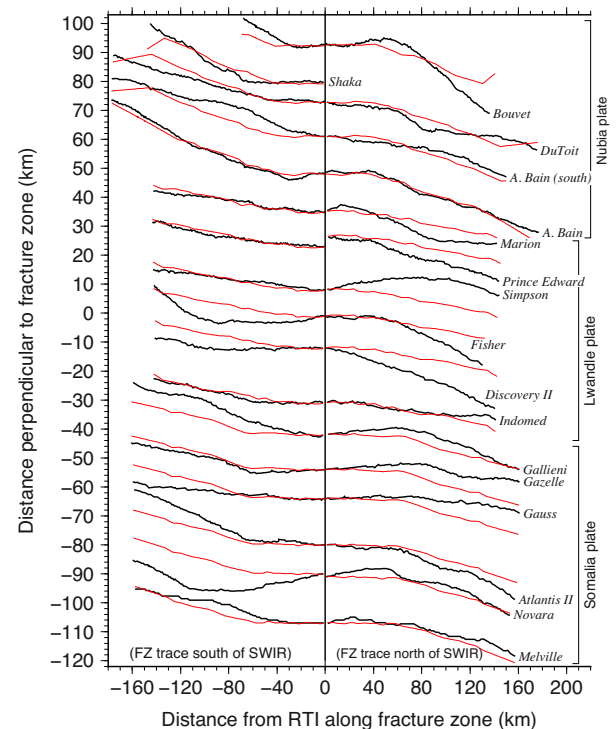

Figure 12. Summary of observed (black) and predicted (red) fracture zone traces from Figs 10, 15 and 18, and Supporting Information Fig. S2. Red lines show the flow lines determined from stage rotations that were derived from the best-fitting Nubia–Antarctic, Lwandle–Antarctica and Somalia–Antarctica rotations in Tables 2–4. Horizontal axis depicts linear distance along each fracture zone. Vertical axis shows linear distance orthogonal to each fracture zone. Vertical distances are exaggerated by 2.4 times relative to horizontal distances, thereby exaggerating the misfits and noise in the digitized traces. Positive and negative distances on the horizontal axis indicate parts of the fracture zone that lie on the Africa or Antarctica sides of the SWIR, respectively. Distances are measured relative to the locations of the northern and southern ridge-transform fault intersections (RTIs), where each fracture zone begins. Transform faults, which are located between the northern and southern RTIs, are omitted from this plot and are instead shown in Fig. 11.

4.4.4 Transform fault small circles and reconstructed fracture zone flow lines

Lwandle–Antarctic plate motion is constrained by the Marion, Prince Edward, Simpson, Fisher, Discovery II and Indomed transform faults and fracture zones. The 657 crossings of these six transform faults are well fit by small circles around the Lwandle–Antarctic C1n pole (Figs 11 and 15) and have a wrms misfit of 1.23 km, ∼40 per cent smaller than their assigned uncertainties. The largest misfit occurs at the northern end of the Discovery II transform fault (Fig. 11), where we may have misidentified the position of the active trace of the transform fault.

Although the traces of the six Lwandle–Antarctic fracture zones differ from each other substantially when compared in detailed (Fig. 12), all six share one common attribute, namely, they have anticlockwise bends (Figs 12, 15 and 18) that are evidence for an anticlockwise rotation of the plate slip direction since 20 Ma. The varying misfits of the modelled flow lines to the digitized fracture zone traces (Fig. 12) reflect the best compromise fit of the rotation sequence to the different fracture zone geometries. Larger misfits for the Simpson, Fisher and Discovery II fracture zones may indicate that we misidentified the locations of the paleo-shear zone along

Table 3. Lwandle–Antarctic best-fitting finite rotations.

Chron	DOF	Lat.	Long.	Ω	Rotation covariances*					
		(°N)	(°E)	(°)	a	b	c	d	e	f
1n*	798	5.81	315.96	−0.095	13.1	8.7	−15.2	8.7	−12.3	19.5
2n	128	12.58	310.65	−0.208	11.2	0.5	−8.0	7.4	−7.0	36.3
2An.1	139	10.57	316.50	−0.331	11.1	−2.6	1.0	10.4	−15.1	56.1
2An.3	112	6.95	320.13	−0.432	13.3	5.3	−5.2	8.0	−5.6	27.4
3n.1	79	8.78	319.34	−0.497	30.5	0.1	−21.5	14.4	−10.5	62.0
3n.4	101	5.57	323.62	−0.622	34.0	9.8	−23.4	15.7	−15.2	42.3
3An.1*	92	5.15	323.80	−0.749	155.7	112.5	−185.8	88.6	−139.6	229.6
3An.2*	81	8.49	321.19	−0.843	201.5	143.6	−234.8	110.4	−174.0	284.5
4n.1	52	13.88	315.02	−0.925	88.1	27.0	−86.0	53.7	−28.5	216.8
4n.2	63	6.03	324.07	−1.020	54.6	13.5	−34.7	63.7	−46.2	111.8
4A	123	9.01	321.52	−1.159	22.1	6.7	−11.8	13.6	4.9	95.9
5n.1	129	12.50	318.04	−1.274	32.4	4.6	−0.2	24.0	19.7	125.1
5n.2	156	10.12	321.57	−1.448	39.0	15.0	2.9	24.4	23.4	110.2
5An.2	104	7.57	324.08	−1.630	91.4	−8.9	−13.4	103.9	26.3	128.5
5AC	124	7.50	324.20	−1.872	77.1	25.4	−9.2	65.8	23.3	145.0
5AD	81	8.94	322.98	−2.006	144.3	−22.1	−7.1	75.5	2.5	140.2
5Cn.1*	37	8.84	323.52	−2.088	364.6	217.0	−328.7	226.7	−281.9	384.0
5D	116	9.52	323.04	−2.294	261.7	−86.2	−101.8	101.9	45.0	161.9
5E	102	10.73	321.66	−2.460	69.6	16.7	−25.3	44.9	19.2	201.5
6ny	60	11.70	320.89	−2.542	207.1	51.5	−146.3	101.1	−64.3	402.2
6no	65	12.03	320.79	−2.629	141.1	−46.8	−41.1	322.1	76.5	376.7

These finite rotations reconstruct movement of the Lwandle plate relative to the Antarctic plate and include corrections for 2 km of outward displacement described in the text. The rotation angles Ω are positive CCW. Each rotation is the mean of 1000 bootstrap solutions (see the text).

*The rotations marked with an asterisk have covariances that were determined from the geometric distribution of the observations using the method of Chang (1988). All other covariances are determined from the bootstrapping procedure described in the text. DOF, the degrees of freedom, equals the total number of anomaly, transform fault and fracture zone flow-line crossings used to estimate the rotation for a given time reduced by the number of estimated parameters. The wrms misfits for these rotations are given in Table 1. The Cartesian rotation covariances are calculated in a Lwandle-fixed reference frame and have units of 10^{-9} radians^2. See Table 2 footnotes for further information about the rotation covariances.

portions of these three fracture zones. Alternatively, it may indicate that their fracture zones wandered along-strike in response to ridge propagation at their paleo-ridge-transform intersections.

The wrms misfits to the 1254 Lwandle–Antarctic fracture zone crossings increase gradually from 0.3 km for the youngest segments of the fracture zones to 3–4 km for segments older than C5n.2 (Table 1). $\hat{\kappa}$ is 0.81 for the fracture zone crossings, indicating that the wrms misfit is ≈10 per cent larger than the uncertainties we assigned to the fracture zone crossings. Given the close agreement between the two, we did not further adjust the fracture zone uncertainties.

The fracture zone flow lines predicted with the noise-reduced Lwandle–Antarctic rotations differ insignificantly from the flow lines estimated from the best-fitting rotations (compare red and aquamarine flow lines in Fig. 15), as do the wrms misfits for the two sets of rotations. As is described in Section 4.6, the noise-reduced rotations predict more smoothly varying interval directions than is the case for the best-fitting rotations and thus probably better approximate Lwandle–Antarctic slip directions since 20 Ma than do the best-fitting rotations.

4.5 Somalia–Antarctic plate motion

4.5.1 Best-fitting rotations

The best-fitting Somalia–Antarctic rotations (Table 4) were determined from a simultaneous inversion of 1987 magnetic reversal crossings between the Gallieni transform fault and Rodriguez triple junction, 397 crossings of six transform faults and 1396 crossings of six fracture zones (Table 1). Each rotation is calibrated for 2 km

of outward displacement (Fig. 5), the same as for the Lwandle–Antarctic plate rotations.

The Somalia–Antarctic poles are clustered within several angular degrees of 8°N, 42°W (Fig. 16A), close to the Lwandle–Antarctic pole locations (Fig. 13A). The poles for progressively younger reversals migrate slowly southwards, consistent with an anticlockwise change in the plate slip direction through time.

The age-progression of best-fitting Somalia–Antarctic rotation angles (Fig. 16C) is less noisy than for the Nubia–Antarctic and Lwandle–Antarctic plate pairs (Figs 7C and 13C), most likely because we were able to identify with confidence the magnetic reversal sequence and paleoridge geometry from the dense, well-navigated magnetic track coverage of the Somalia–Antarctic segment of the SWIR. The best-fitting and noise-reduced rotation angles define at least one change in the angular rotation rate since 20 Ma. A description of Somalia–Antarctica interval velocities is deferred until Section 4.6.

4.5.2 Noise-reduced rotations from REDBACK

Noise-reduced rotations for the Somalia–Antarctica plate pair are given in Supporting Information Table S3 and are illustrated in Figs 16(B) and (C). The path described by the noise-reduced poles is smoother and the poles more tightly grouped than for the best-fitting poles (Fig. 16B), as expected. Southward migration of the noise-reduced poles with time is consistent with an anticlockwise change in the plate slip direction since 20 Ma. The well-constrained, smoothly varying, noise-reduced angles also indicate that motion has changed at least once since 20 Ma, most likely near 8 Ma (Fig. 16C).
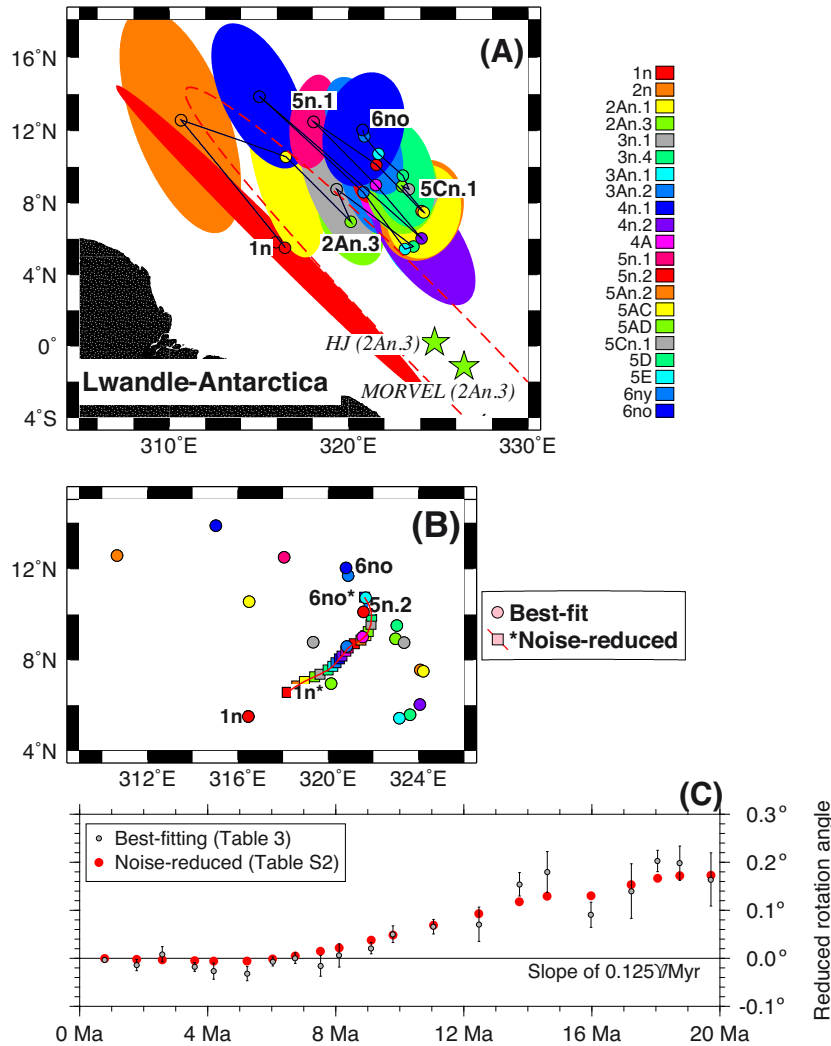
Figure 13. Lwandle–Antarctic finite rotation poles (A,B) and angles (C). (A) Best-fitting poles with 2-D 95 per cent confidence regions (Table 3). Green stars show the locations of the MORVEL and Horner-Johnson *et al.* (2007) poles for C2An.3. Red ellipse is the MORVEL 2-D 95 per cent pole uncertainty region. Panels (B) and (C) compare the Lwandle–Antarctica best-fitting finite opening poles and angles (Table 3) to noise-reduced poles and angles (Supporting Information Table S2). Selected anomalies are labelled to facilitate the comparison. The rotation angles are reduced by a slope of 0.120° Myr^{-1} to facilitate the comparison.

4.5.3 Magnetic reversal reconstructions

The well-mapped magnetic anomalies, transform faults and fracture zones from the Somalia–Antarctic plate boundary reliably constrain all 21 rotations for this plate pair. In particular, the superb magnetic and bathymetric mapping of the seafloor from numerous, closely spaced ship-track lines east of 61°E (Fig. 17) allowed us to identify all 21 magnetic reversals and the paleoridge segmentation along much of the eastern third of the plate boundary. Near the western end of the Somalia–Antarctic plate boundary (54-57°E), numerous crossings of chrons 1n through 5An.2 from two well-surveyed spreading segments immediately west of the Atlantis II transform fault (Supporting Information Fig. S4) strongly constrain our reconstructions for chrons 1n through 5An.2. Closely spaced magnetic profiles across the spreading segment at the north end of the Atlantis II transform fault (Hosford *et al.* 2003; Baines *et al.* 2007) constrain the reconstructions out to C6no (Supporting Information Fig. S5). Our reconstructions are constrained by relatively few identifications of magnetic anomalies between 66°E and the Rodriguez Triple Junction (70°E), which became progressively more difficult

to identify toward the Rodriguez Triple Junction, possibly because seafloor spreading rates become progressively slower toward the triple junction.

The wrms misfit of the best-fitting rotations to the 1987 Somalia–Antarctic reversal crossings is 1.51 km, nearly the same as for the other two plate pairs (i.e. 1.55 and 1.67 km). The noise-reduced rotations increase the wrms misfit to 1.55 km, with a maximum misfit increase of 0.3 km for the hard-to-identify C5AD. The small increase in misfit (only 40 m) is an excellent tradeoff for the less-noisy rotation sequence that is identified by REDBACK.

4.5.4 Transform fault small circles and reconstructed fracture zone flow lines

The traces of all six transform faults that offset the Somalia–Antarctic segment of the SWIR are well fit by small circles around the C1n pole (Figs 11 and 18). The wrms misfit to the 397 transform fault crossings is 1.0 km, nearly the same as for the Nubia–Antarctic (0.92 km) and Lwandle–Antarctic (1.23 km) plate pairs.
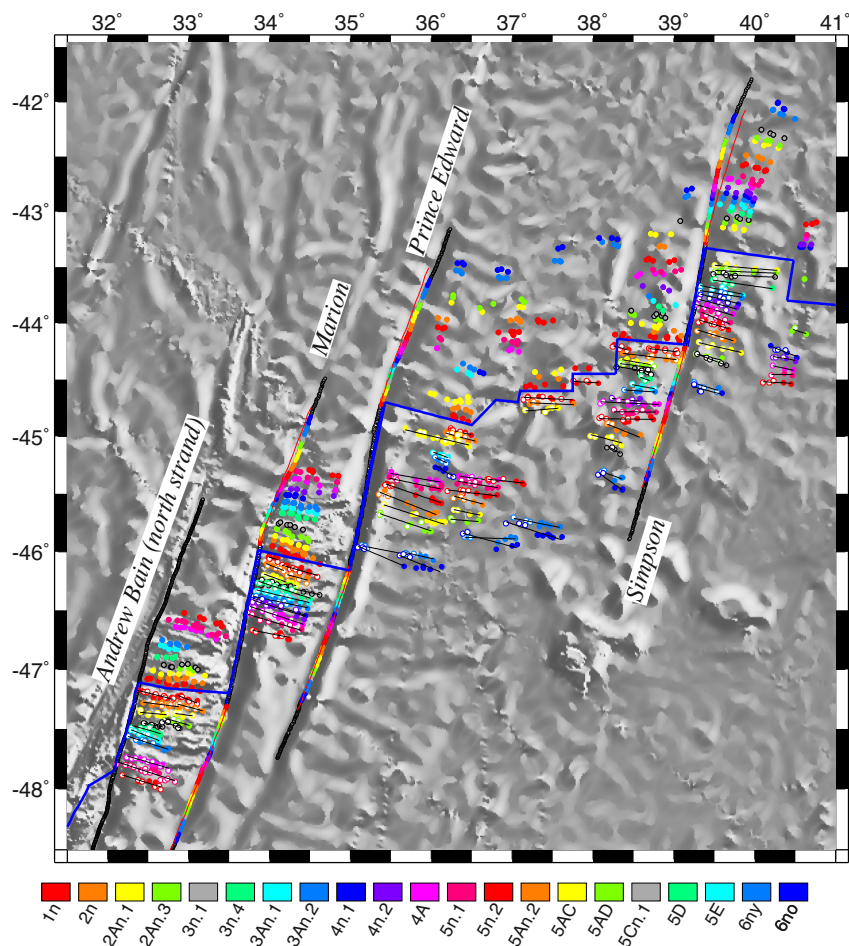
Figure 14. Best-fitting reconstructions of Lwandle–Antarctic magnetic lineations. Solid circles show unrotated magnetic reversal crossings identified from shipboard and airborne data (also shown in Fig. 2). Open circles show Lwandle plate reversal crossings rotated onto the Antarctic plate. Black lines show great circle segments that best fit the reconstructed reversal crossings, which define paleospreading segments. The blue line shows the present plate boundary. See Fig. 2(A) for the map location.

All six fracture zones that are used to estimate the Somalia–Antarctic rotations bend anticlockwise at distances of 40–80 km from their ridge-transform intersections (Figs 12 and 18), similar to the bends in the Lwandle–Antarctic fracture zones and consistent with an anticlockwise change in the Somalia–Antarctic direction since 20 Ma. Except for the southern, Antarctic portion of the Novara fracture zone, the digitized traces of the fracture zones are well fit by synthetic flow lines (Figs 12 and 18, and Supporting Information Fig. S4). The wrms misfits increase slowly from only 140 m for C1n to 4.8 km for C6no (Table 1), consistent with the age-progressive increase in misfit observed for the other SWIR fracture zones. A ~10 km systematic difference between the modelled flow line and digitized trace for the Antarctic-plate portion of the Novara fracture zone (Fig. 18) suggests that we misinterpreted the location of the fracture zone within the valley. Despite the poor fit, the best-fitting rotations are influenced relatively little by the trace of the Novara fracture zone because the uncertainties assigned to the southern portion of the Novara fracture zone are ≈2–3 times larger than for the Atlantis II and Melville fracture zones (Fig. 18), whose traces are partly constrained by multibeam or other detailed bathymetric data.

The wrms misfit (2.83 km) of flow lines predicted by the noise-reduced stage rotations to the digitized fracture zone traces is only 0.04 km (40 m) greater than the wrms misfit for the best-

fitting rotations (Fig. 18). The noise-reduced rotations thus predict a smoother and hence more physically realistic description of Somalia–Antartica plate motion than do the best-fitting rotations without significantly degrading the fit to the underlying observations.

4.6 Quaternary and Neogene Southwest Indian Ridge plate kinematics

We now describe the evolution of Nubia–Antarctic, Lwandle–Antarctic and Somalia–Antarctic plate motions since 20 Ma using their best-fitting finite rotations (Tables 2–4), the noise-reduced finite rotations (Supporting Information Tables S1–S3) and the noise-reduced stage angular velocities (Supporting Information Tables S4–S6). We use two complementary approaches for the analysis. From the stage angular velocities for each plate pair, we predict interval seafloor spreading rates and plate slip directions at a central location along each plate boundary. This familiar approach is effective for identifying the timing of plate motion changes, but reduces the inherently three-dimensional information that is embedded in a rotation to a two-dimensional linear velocity at a single point on the plate boundary. We therefore also decompose each finite rotation into three orthogonal component angles in order to discriminate
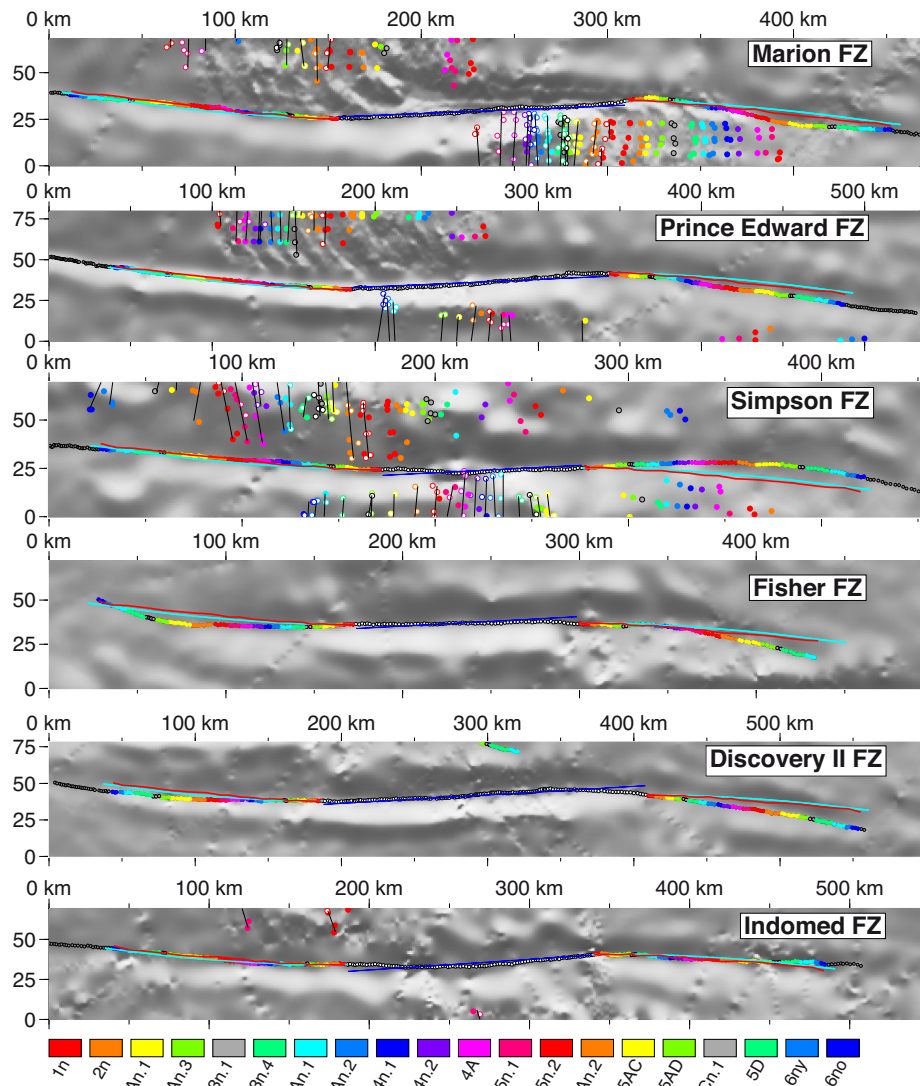
Figure 15. Digitized traces and modelled flow lines for Lwandle–Antarctica fracture zones and transform faults. All coloured circles identify fracture zone crossings used to constrain the Lwandle–Antarctica rotations. Open circles identify transform fault crossings that constrain the C1n rotation. The red and aquamarine flow lines are predicted by stage rotations derived from the best-fitting rotations in Table 3 and the noise-reduced stage angular velocities in Supporting Information Table S5. Blue lines show small-circle fits for the youngest (C1n) opening pole to the actively slipping, transform fault segment of each flow line. A colour legend for the reversal and fracture zone crossings appears below the maps. Maps are oblique Mercator projections about the Somalia–Antarctica opening pole from Lemaux *et al.* (2002) for C5n.2.

between changes in plate opening rates, plate slip directions and the opening gradient along a plate boundary. The orthogonal component angles for a given rotation are estimated by projecting the finite rotation onto an alternative set of coordinate axes that are defined such that one axis (Axis B) coincides with the geographic centre of the plate boundary (e.g. Fig. 19A), a second axis (Axis A) is located 90 angular degrees from Axis B along a great circle that connects Axis B and the pole of rotation and the third axis (Axis C) is orthogonal to Axes A and B (Wilson 1993). Component angle A quantifies uniform opening across a spreading centre, whereas Component angle B controls the degree of magnetic anomaly fanning along a spreading centre. Component angle C equals zero if the finite rotation pole lies within the plane defined by Axes A and B, but acquires non-zero values if the pole of rotation migrates out of the A–B plane due to a change in the direction of plate motion. During periods of steady plate motion, the component angles parallel to Axes A and B change linearly with time. Departures from

linear changes in these two component angles are thus proxies for boundary-wide changes in plate opening rates and changes in the opening gradient, respectively. Non-zero values for the C component angles are a proxy for boundary-wide changes in plate slip directions.

Although the above methodology requires that we approximate the finite rotations as Euler vectors, the approximation introduces errors that are no larger than 5 per cent for finite rotation angles that are smaller than 3°, a condition satisfied by all of the rotations in this study (Tables 2–4 and Supporting Information Tables S1–S3). The uncertainty in each component angle is determined by transforming a rotation's covariances into the new coordinate system and selecting the appropriate component variance.

Except where noted, we consider interval velocities estimated from the noise-reduced stage angular velocities to be more accurate than the interval velocities that are estimated from the noisier best-fitting rotations. The former maximize the temporal resolution of

Table 4. Somalia–Antarctic best-fitting finite rotations.

Chron	DOF	Lat.	Long.	Ω	Rotation covariances*					
		(°N)	(°E)	(°)	*a*	*b*	*c*	*d*	*e*	*f*
1n*	601	5.02	316.55	−0.097	14.1	24.2	−17.7	45.9	−32.6	23.5
2n	172	6.31	317.48	−0.221	29.0	44.8	−34.4	84.2	−68.3	69.1
2An.1	179	8.74	316.09	−0.308	20.1	24.8	−22.3	46.8	−39.4	59.3
2An.3	158	6.85	316.97	−0.423	20.6	23.4	−32.0	54.0	−60.0	115.4
3n.1	106	6.86	318.60	−0.498	55.2	61.6	−47.9	126.5	−94.6	162.2
3n.4	113	3.48	323.67	−0.604	44.1	37.2	−48.4	115.1	−130.1	245.1
3An.1	86	4.15	323.08	−0.701	39.6	49.8	−57.1	132.1	−145.6	216.1
3An.2	75	4.25	322.60	−0.780	54.4	78.4	−82.6	199.8	−199.0	272.8
4n.1	83	7.91	317.61	−0.898	94.6	140.4	−137.6	251.2	−236.6	274.4
4n.2	73	4.21	322.78	−0.953	71.4	97.5	−109.3	176.2	−178.3	255.9
4A	147	6.06	320.41	−1.107	35.4	47.8	−47.9	111.9	−104.6	135.1
5n.1	151	8.71	316.90	−1.218	24.8	33.5	−36.2	93.6	−86.8	96.7
5n.2	201	7.53	320.33	−1.383	12.7	14.4	−19.0	33.2	−43.2	97.0
5An.2	148	6.12	323.44	−1.554	47.2	32.1	−25.9	75.2	−54.0	145.8
5AC	136	6.92	323.68	−1.724	45.9	47.6	−23.6	151.0	−123.1	292.5
5AD	97	7.75	322.74	−1.839	102.8	180.3	−166.4	432.0	−379.7	518.0
5Cn.1	148	7.89	322.96	−2.060	70.4	29.3	−42.4	119.2	−107.9	383.7
5D	94	8.35	322.40	−2.206	44.1	29.4	−24.5	152.1	−179.7	335.8
5E	102	9.52	320.79	−2.354	58.5	31.0	32.8	103.6	−101.3	458.1
6ny	102	10.44	319.84	−2.474	83.2	41.6	−15.0	84.1	−45.9	92.7
6no	277	11.17	319.06	−2.621	42.8	24.8	34.6	49.3	27.0	87.9

These finite rotations reconstruct movement of the Somalia plate relative to the Antarctic plate and include corrections for 2 km of outward displacement described in the text. The rotation angles Ω are positive CCW. Each rotation is the mean of 1000 bootstrap solutions (see text).

*Rotations that are marked with an asterisk have covariances that were determined from the geometric distribution of the observations using the method of Chang (1988). All other covariances are determined from the bootstrapping procedure described in the text. DOF, the degrees of freedom, equals the total number of anomaly, transform fault and fracture zone flow-line crossings used to estimate the rotation for a given time reduced by the number of estimated parameters. The wrms misfits for these rotations are given in Table 1. The Cartesian rotation covariances are calculated in a Somalia-fixed reference frame and have units of 10^{-9} radians^2. See Table 2 footnotes for further information about the rotation covariances.

the underlying data and describe a smoother kinematic history than do the latter without significantly degrading the fit to the original data.

4.6.1 Nubia–Antarctica

The orthogonal component angles and stage velocities for the Nubia–Antarctic plate pair (Figs 19 and 20) clearly indicate that the rate and direction of plate motion have remained steady since ∼7 Ma. The interval opening rates since ∼7 Ma near the centroid of the plate boundary have varied by no more than 5 per cent from 13.5–14.5 mm yr^{-1} (Fig. 20A) and the direction has varied by no more than 1°–2° (Fig. 20B). Within their 1–σ uncertainties, component angles A and B have both changed linearly since ≈7 Ma and component angles C have not varied from values of zero. These indicate that the pole and angular rotation rate have not changed during this period.

Two of the three component angles clearly reveal a change in plate motion at ≈7 Ma, consisting of a ∼20 per cent opening-rate slowdown (Fig. 19A) and ∼5° anticlockwise rotation of the plate slip direction (Fig. 19C). Greater noise in the best-fitting interval rates for times before 8 Ma is caused by the previously described difficulty in identifying reversals older than C5An.2 (Section 4.3.3).

Although interval spreading directions from 20 to 8 Ma remained remarkably steady (Fig. 20B), our newly estimated rotations predict that seafloor spreading rates before 16 Ma were significantly faster than from 15 Ma to 10 Ma (Figs 19A and 20A). The accuracy of the interval spreading rates from 19.2 to 16 Ma however depends on our reconstructions of a handful of possibly unreliable identifications of C6no, C6ny and C5Cn.1 (Section 4.3.3). Caution is thus

warranted, although we note that the faster spreading rates predicted for times before 16 Ma are consistent with kinematic evidence that is presented in Section 5 for faster SWIR spreading rates before 20 Ma.

In Section 4.7, we test rigorously for the timing of the motion change that is apparent in the component angles and interval velocities.

4.6.2 Lwandle–Antarctica

The orthogonal rotation components determined from the noise-reduced Lwandle–Antarctic rotations are significantly less scattered than are the component angles that we determined from the best-fitting rotations (compare red and grey circles in Fig. 21). The component angles clearly define an opening-rate slowdown at 8–5 Ma (Fig. 22) and anticlockwise change in plate slip direction. At a central location along the Lwandle–Antarctic plate boundary, spreading rates have averaged 13–14 ± 1 mm yr^{-1} (95 per cent) since 5 Ma (Fig. 22A), ∼15 per cent slower than the 15.5 ± 0.5 mm yr^{-1} rate before 8 Ma. The estimated changes in Lwandle–Antarctic plate motion since 20 Ma are remarkably similar to the changes observed for the Nubia–Antarctica plate pair even though the kinematic histories for the two plate pairs are derived from independent observations. These similarities suggest a common cause for the change in motion.

4.6.3 Somalia–Antarctica

The well-constrained best-fitting and noise-reduced orthogonal component angles for the Somalia–Antarctic plate pair clearly
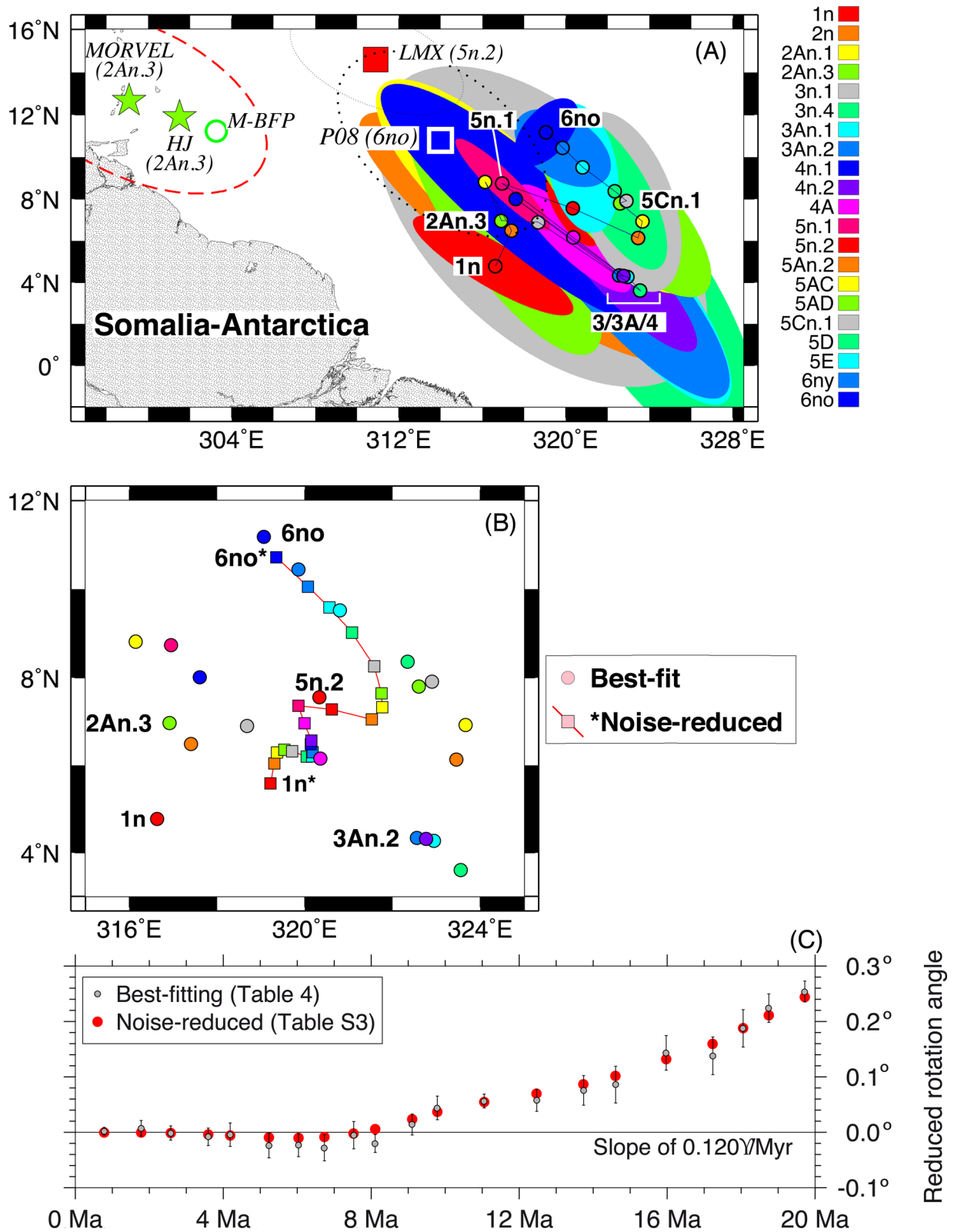
Figure 16. Somalia–Antarctica finite rotation poles (A,B) and angles (C). (A) Best-fitting poles with 2-D 95 per cent confidence regions (Table 4). Green stars show the locations of the MORVEL and Horner-Johnson *et al.* (2007) poles for C2An.3, which are constrained to consistency with closures of regional and global plate circuits. Red ellipse is the MORVEL 2-D 95 per cent pole uncertainty region. The pole labelled 'M-BFP', which best fits the MORVEL Somalia–Antarctic data, is independent of plate circuit closures. Red and blue squares and their 2-D 95 per cent ellipses are the C5n.2 and C6no poles from Lemaux *et al.* (2002) (LMX) and Patriat *et al.* (2008) (P08), respectively. Panels (B) and (C) compare the Somalia–Antarctica best-fitting finite opening poles and angles (Table 4) to noise-reduced poles and angles (Supporting Information Table S3). Selected anomalies are labelled to facilitate the comparison. The rotation angles are reduced by a slope of $0.120°$ Myr^{-1} to facilitate the comparison.
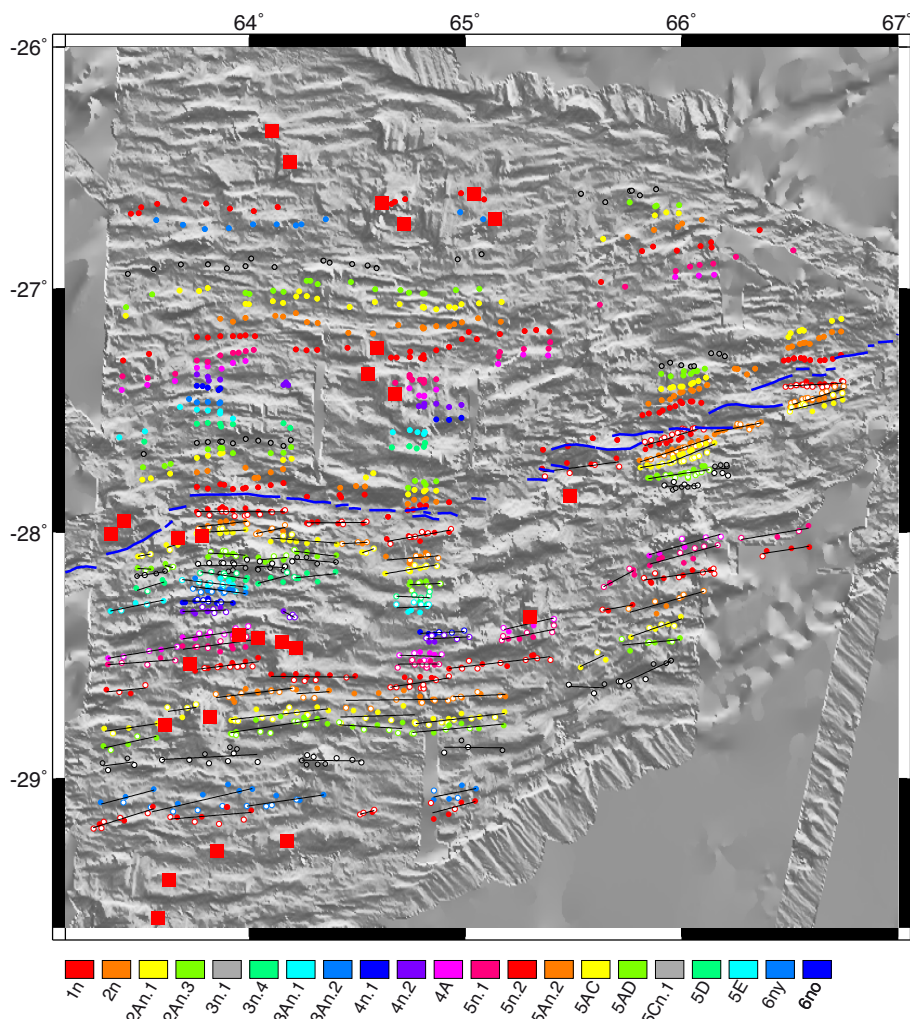
Figure 17. Best-fitting reconstructions of Somalia–Antarctic magnetic lineations. Solid circles show unrotated magnetic reversal crossings identified from shipboard and airborne data (also shown in Fig. 2A). Open circles show Somalia plate reversal crossings rotated onto the Antarctic plate. Black lines show great circle segments that best fit the reconstructed reversal crossings. The blue line shows the present plate boundary. See Fig. 2(A) for map location. Red squares show locations of corrugated surfaces on the footwalls of axial detachment faults identified by Cannat *et al.* (2009).

suggest that seafloor spreading rates and plate slip directions were steady from 20 to 8 Ma (Figs 23A and C), but changed at ∼8 Ma. Before 8 Ma, the opening rate and plate slip direction near the Atlantis II fracture zone averaged 15.2 ± 0.5 mm yr^{-1} and N07-07.5°E ± 2° (Fig. 24). Since then, the spreading rate and direction have averaged 13 ± 0.5 mm yr^{-1} and N01.5°E ± 1°, respectively (Fig. 24), ∼15 per cent slower than and ∼5° anticlockwise from the previous motion. The similarities of the timing and changes in motion to those described for the Lwandle–Antarctica and Nubia–Antarctica plate pairs once again suggest that the changes had a common cause.

From a multibeam survey of 0–26 Myr-old SWIR seafloor between 61°E and 67°E, Cannat *et al.* (2006) measured the azimuths of corrugations on the surfaces of axial detachment faults (identified by the red squares in Fig. 17). Along segments of the SWIR where orthogonal spreading occurs, as appears to be the case for seafloor created between 62° and 65.5°E, the corrugation azimuths should parallel the direction of plate motion at the time that the megamullions formed. We therefore compared the azimuths to our predicted interval plate slip directions as an independent check on the accuracy of our new Somalia–Antarctica rotation sequence (Fig. 25).

Encouragingly, four of the five corrugation azimuths measured on megamullions that are younger than 5 Ma agree to within ±0.5° with the azimuths predicted by our noise-reduced stage rotations (Fig. 25). This suggests that our new rotations accurately describe the direction of motion since 5 Ma. The azimuths of older fault corrugations (20–8 Ma) are rotated ∼2°–3° anticlockwise from the directions predicted by our model, within our model uncertainties. We interpret this as evidence that the errors in paleoslip directions that are predicted by our new Somalia–Antarctic rotations are unlikely to be larger than ∼3°.

4.7 Timing of plate motion changes

Fig. 26 summarizes results from two tests that we used to determine the best timing of plate motion changes for each plate pair. One is based on our REDBACK software analysis, which reports probabilities as a function of rotation age that one or more changes in the pole location or angular rotation rate occurred within the finite rotation sequence (Iaffaldano *et al.* 2014). The other is based on fitting the best-fitting orthogonal component angles with a series of
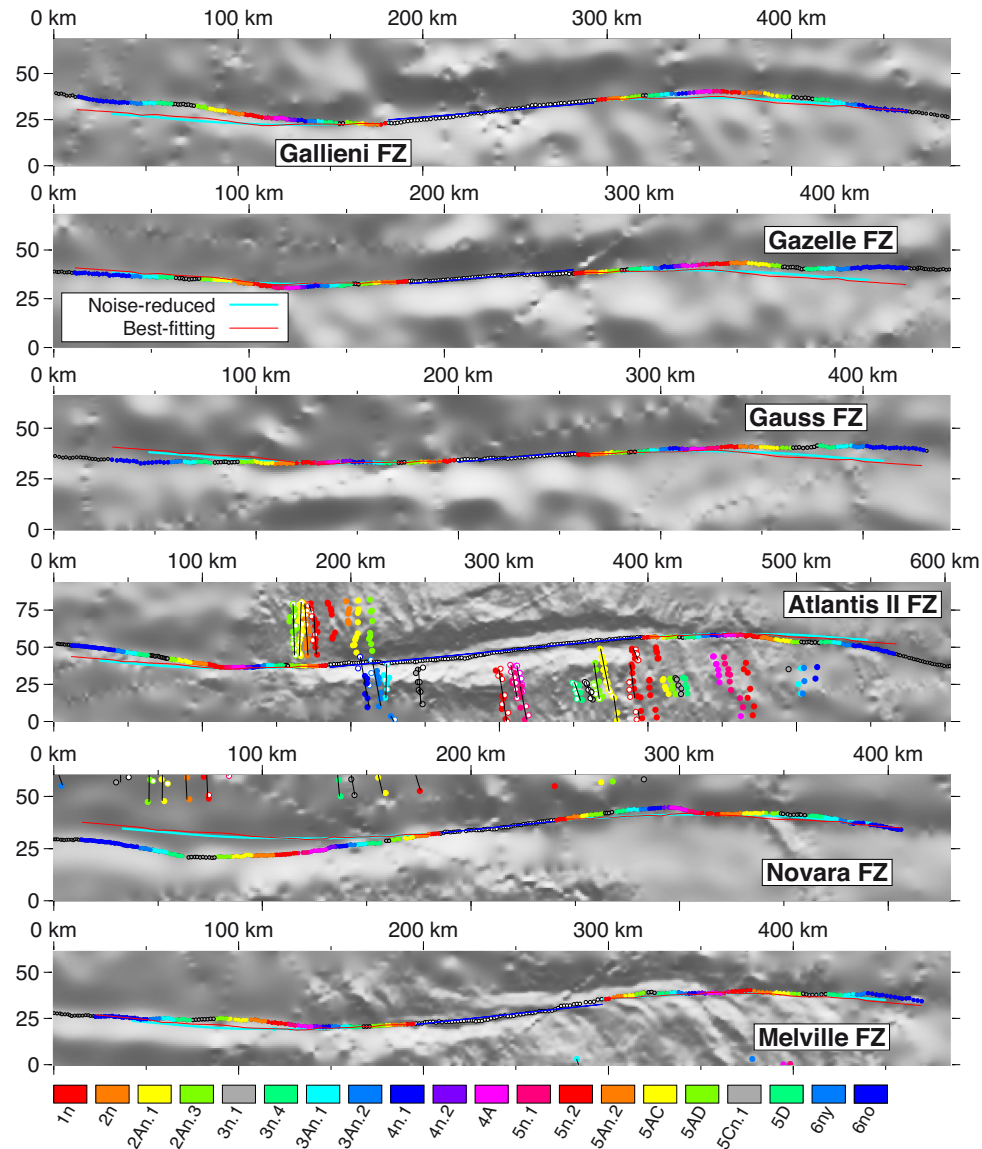
Figure 18. Digitized traces and modelled flow lines for Somalia–Antarctica fracture zones and transform faults. All coloured circles identify fracture zone crossings used to constrain the Somalia–Antarctica rotations. Open circles identify transform fault crossings that constrain the C1n rotation. The red and aquamarine flow lines are predicted by stage rotations derived from the best-fitting rotations in Table 4 and the noise-reduced stage angular velocities in Supporting Information Table S6. Blue lines show small-circle fits for the youngest (C1n) opening pole to the actively slipping, transform fault segment of each flow line. A colour legend for the reversal and fracture zone crossings appears below the maps. Maps are oblique Mercator projections about the best Somalia–Antarctica opening pole for C5n.2 from Lemaux *et al.* (2002).

models that enforce different possible times for a single change in motion. The results from each are described and compared below.

Our REDBACK analysis of the Nubia–Antarctic finite rotations defines one or possibly two changes in motion (Fig. 26D). The most likely is a change in the angular rotation rate at ∼6.5–7 Ma, consistent with the timing suggested by a simple visual inspection of the component angles (Fig. 19) and interval velocities (Fig. 20). The REDBACK analysis also suggests a possible difference between the pole location for C6no and that for younger reversals. We are less confident of that result given concerns about the reliability of our identifications of C6no and the paleoridge segmentation at the western end of the SWIR (Section 4.3.3).

Our REDBACK analysis of the Lwandle–Antarctic best-fitting rotation sequence indicates that a single change in motion occurred at 5.5 Ma (Fig. 26E), ∼1.5 Myr after the change in Nubia–Antarctic

plate motion. The results are however permissive of a change as early as 6.5 Ma or as recently as 4.5 Ma.

Finally, our analysis of the Somalia–Antarctic rotation sequence indicates that one and possibly two changes in the angular rotation rate occurred, the most likely at 6.5–7 Ma and an earlier change at 17 Ma (Fig. 26F). Bounds on the more recent change extend from 8.5 to 6.0 Ma. In Section 5, we discuss the latter change in the context of a change in plate motion that began before 20 Ma (Patriat *et al.* 2008).

We also tested for possible changes in motion using the well-constrained Ω^A and Ω^C component angles, which isolate the components of plate motion related to the ridge-normal opening rates and plate slip directions. Given that changes in both component angles should be linear during periods of steady plate motion, we tested whether the fit of a single slope and intercept to the age
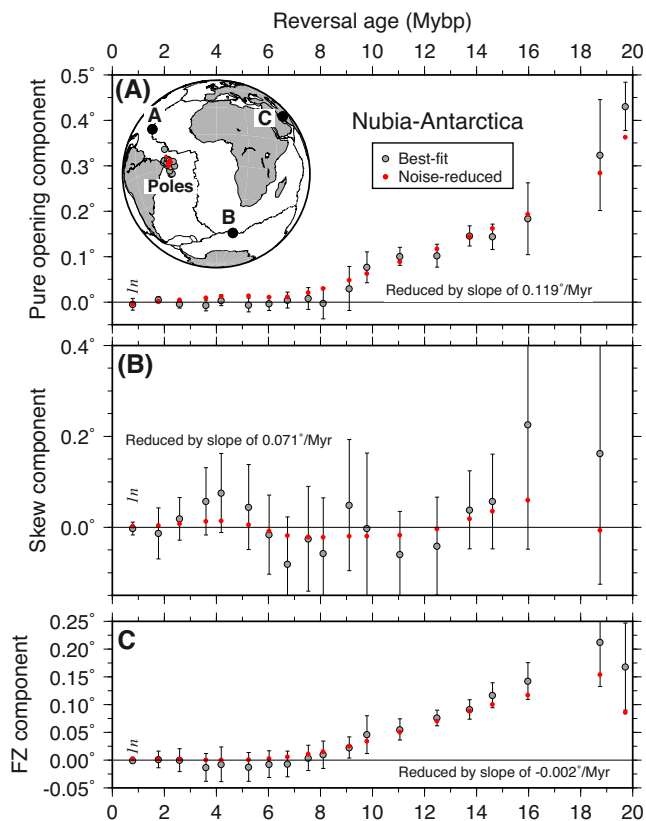
Figure 19. Projections of the Nubia–Antarctica best-fitting (Table 2) and noise-reduced rotations (Supporting Information Table S1) onto Axes A, B and C depicted on the inset globe. Each set of component angles is reduced by the slope that optimizes the fit to the best-fitting component angles for C1n to C4n.1. The slopes defined by the rotation components A and C both change significantly at least once since 20 Ma and are consistent with a slowdown in seafloor spreading rates everywhere along the plate boundary and change in the plate slip direction. Uncertainties are 1-σ.

progression of the component angles is improved significantly if the component angles are instead fit by two slopes and one intercept.

Figs 26(A)–(C) show how the misfits from inversions of the component angles for all three plate pairs change for numerous trial ages for an assumed change in plate motion. The Nubia–Antarctic component angles are best fit by a model that imposes a change in motion at 7.8 Ma, but are permissive of a change as recently as 6.5 Ma (within the 95 per cent confidence limits). Inversions of the Lwandle–Antarctic and Somalia–Antarctic component angles and reversal ages give best change-ages of 5.3 Ma (Fig. 26B) and 7.4 Ma (Fig. 26C). All three agree with their corresponding REDBACK estimates within their 95 per cent confidence limits.

Given the similarity of the change-points for the three plate pairs, we inverted the Ω^A component angles for all three plate pairs while requiring that the change in motion occur simultaneously along all three plate boundaries. The Ω^A component angles isolate most of the information from the well-dated magnetic reversal crossings and thus provide unambiguous information about the timing of plate motions. The simultaneous inversion gives a best age of $7.2^{+0.9}_{-1.4}$ Ma (95 per cent limits) and $\chi^2 = 152.3$. In contrast, separate inversions of the Ω^A component angles for the three plate pairs give respective best-fitting ages for motion changes of 8.1, 5.3 and 7.2 Ma and a summed, least-squares misfits χ^2 of 132.2. An F-ratio comparison of the misfits indicates that the latter, more complex model improves

on the fit of the simultaneous-change model at only the 97 per cent confidence level. Limiting the comparison to the Nubia–Antarctica and Somalia–Antarctica component angles further reduces the significance level to only 77 per cent, with a best change-age of 7.3 Ma and 95 per cent limits of 8.2 Ma and 6.6 Ma.

The observations are thus (weakly) permissive of a simultaneous change in motion for all three plate pairs at $7.2\,\mathrm{Ma}^{+0.9}_{-1.4}$ Ma (95 per cent limits) and are more strongly permissive of a simultaneous change in Nubia–Antarctic and Somalia–Antarctic plate motions at $7.3^{+0.9}_{-0.7}$ Ma (95 per cent limits). We consider it implausible that the Lwandle plate, which shares long boundaries with both the Nubia and Somalia plates, moves independently from them. We thus prefer a model in which the motions of all three plate pairs changed at $7.2^{+0.9}_{-1.4}$ Ma. We cannot however preclude the possibility that Lwandle–Antarctic motion changed more recently than did the motions of the other two plate pairs.

5 DISCUSSION

5.1 Noise-reduced versus best-fitting rotations

Given that best-fitting and noise-reduced rotations are derived above for each of the Nubia–Antarctic, Lwandle–Antarctica and Somalia–Antarctic plate pairs, it behooves us to specify which are preferred for future plate reconstructions. We prefer the noise-reduced rotations given in Supporting Information Tables S1–S6 for two reasons. First, the fitting penalties associated with these rotations are only 0.13, 0.19 and 0.04 km for reconstructed magnetic reversal crossings from the three plate boundaries and fracture zone flow lines predicted by the best-fitting and noise-reduced rotations differ insignificantly. The noise-reduced rotations thus fit the original data nearly as well as do the best-fitting rotations. Second, the interval velocities predicted by the noise-reduced stage angular velocities for all three plate pairs vary more smoothly through time than do those predicted by stage rotations determined from the best-fitting rotations. In contrast, the best-fitting rotations predict occasional, rapid changes in plate motion that are not only kinematically implausible, but are most assuredly a consequence of noise in the underlying data.

5.2 A major SWIR spreading slowdown since 34 Ma

From a comparison of 34–26, 26–20 and 20 Ma-to-present spreading rates estimated from modelling of several magnetic profiles that cross the SWIR at locations east of the Bain fracture zone, Patriat *et al.* (2008) describe a factor-of-two slowdown in spreading rates along the eastern half of the SWIR at ~24.2 Ma. Below, we briefly examine our new results in the context of this spreading-rate slowdown. We also extend this comparison to the western half of the SWIR, where Nubia–Antarctic plate motion is accommodated. To accomplish this comparison, we combine finite and stage rotations from Cannat *et al.* (2006), Patriat *et al.* (2008) and Cande *et al.* (2010) for times older than Chron 6 (19.2 Ma) with our own rotations.

Along the Nubia–Antarctic segment of the SWIR, Cande *et al.* (2010) estimate a finite rotation for C13o (33.705 Ma) partly from seven crossings of C13 between 15°E and 25°E. A stage rotation that we determined from their C13o finite rotation and our Nubia–Antarctic rotation for C6no predicts that seafloor spreading rates at 20.0°E averaged 22.7 ± 0.5 mm yr⁻¹ from 33.7 to 19.7 Ma (red circle in Fig. 27A). Seafloor spreading rates after 19.7 Ma decreased
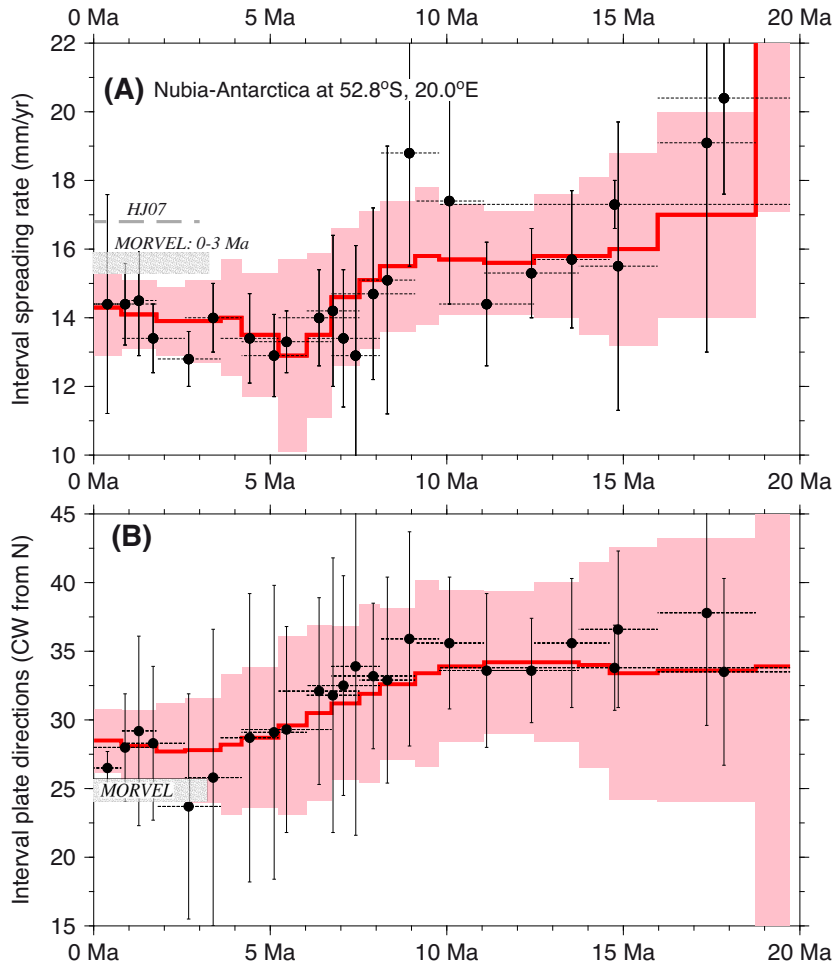
Figure 20. Nubia–Antarctic plate interval velocities at 52.8°S, 20.0°E, the approximate midpoint of the Nubia–Antarctic plate boundary. Black circles show interval rates and directions determined from stage rotations that we derived from the best-fitting finite rotations in Table 2. These average plate motion over 1-Myr-long to 3-Myr-long intervals, as indicated by the horizontal dashed lines that are centred on the circles. The red line and pink-shaded area show interval velocities and nominal 1-σ uncertainties determined with the noise-reduced stage rotations from Supporting Information Table S4. (A) Interval seafloor spreading rates. Grey bar is centred on the 3-Myr-average MORVEL Nubia–Antarctica estimate and encompasses its 1-σ uncertainty. The interval rates use magnetic reversal age estimates from Table 1. 'HJ07' identifies the 3-Ma-average rate predicted by the Nubia–Antarctic angular velocity of Horner-Johnson *et al.* (2007). (B) Nubia–Antarctica interval directions. Grey bar shows the MORVEL estimate and encompasses its 1-σ directional uncertainty.

by ∼40 per cent to ∼16 mm yr^{-1} at this location (Fig. 27A) and decreased an additional ∼20 per cent at 7.2 Ma$_{-1.4}^{+0.9}$ Ma (see previous section and Fig. 27A). A significant slowdown in seafloor spreading thus occurred after 34 Ma along the western half of the SWIR, coinciding with the slowdown along the eastern SWIR. The timing and magnitude of the spreading-rate slowdown before 20 Ma cannot be documented in more detail due to the absence of any published reconstructions of magnetic reversals from the western half of the SWIR that are intermediate in age between Chrons 6 and 13.

Along the SWIR east of 32°, we estimated interval spreading rates for times between 34 Ma and 20 Ma from the following rotations: (1) Cannat *et al.* (2006) estimate stage rotations for 25.987–23.295 Ma (Chrons 8n.2 to 6Cn.3) and 23.295–19.722 Ma (Chrons 6Cn.3 to 6no) from dense magnetic data east of ∼61°E, (2) Patriat *et al.* (2008) estimate finite rotations for C6no, C8n.2 and C13, which we combined to determine 33.705-to-25.987 Ma (C13o-C8n.2) and 25.987-to-19.72 Ma (C8n.2-C6no) stage rotations, (3) Cande *et al.*'s (2010) reconstruction of C13o is derived partly from ∼25 crossings of C13 east of the Bain fracture zone. We combined their C13o finite rotation with our C6no Somalia–Antarctic finite rotation to determine a 33.705-to-19.72 Ma stage rotation

The Somalia–Antarctic interval velocities predicted by the above stage rotations (Fig. 27B) clearly show the major spreading-rate slowdown described by Patriat *et al.* (2008). The slowdown is robust with respect to the averaging interval that is selected and the source of the reconstructions. The interval rates predicted by Cannat *et al.*'s 2–3-Myr-long stage rotations suggest that the slowdown was even larger than estimated by Patriat *et al.* (2008). The pattern of interval spreading rates shown in Fig. 27(B) suggests that the slowdown may have been more gradual than inferred by Patriat *et al.* (2008) and may have ended as recently as ∼18 Ma, somewhat later than the ∼24 Ma date estimated by Patriat *et al.*

5.3 Motion since 20 Ma: comparison to previous results

5.3.1 Nubia–Antarctica

Previous estimates of Nubia–Antarctica plate motion during the Quaternary and Neogene are limited to Chrons 2A and 5n.2. Motion that is predicted by our new Nubia–Antarctic C5n.2 rotation (Supporting Information Table S1) differs significantly from that predicted by the C5n.2 rotations of Lemaux *et al.* (2002) and
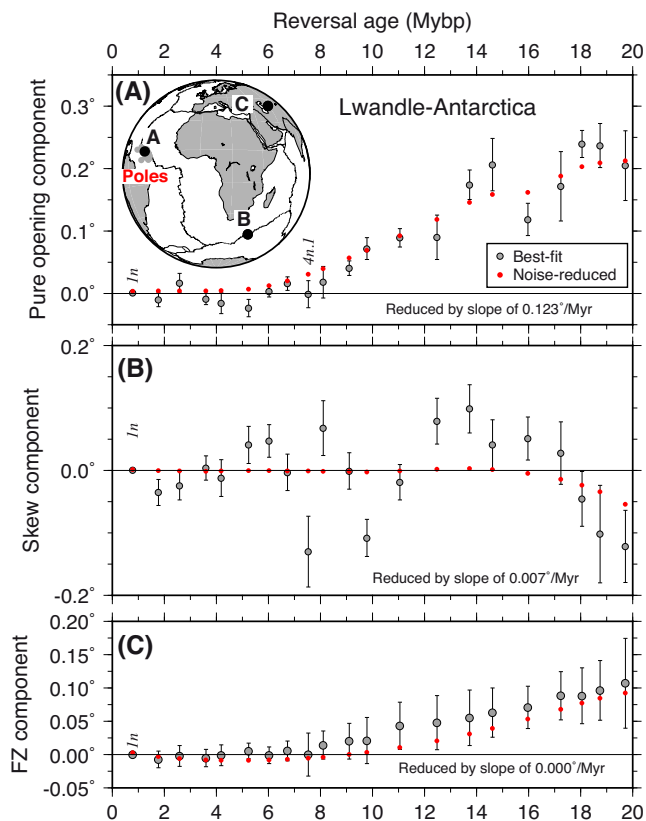
Figure 21. Projections of the Lwandle–Antarctica best-fitting (Table 3) and noise-reduced rotations (Supporting Information Table S2) onto Axes A, B and C depicted on the inset globe. Each set of component angles is reduced by the slope that optimizes the fit to the best-fitting component angles for C1n to C4n.1. The slopes defined by the rotation components A and C both change significantly at least once since 20 Ma, consistent with a slowdown in seafloor spreading rates everywhere along the plate boundary and change in the plate slip direction. Uncertainties are 1-σ.

Royer *et al.* (2006). For example, near the geographic centre of the Nubia–Antarctica plate boundary (52.6°S, 20°E), our C5n.2 Nubia–Antarctic rotation predicts seafloor opening of 159.0 ± 4.9 km (95 per cent uncertainty). At the same location, the C5n.2 rotations of Lemaux *et al.* (2002) and Royer *et al.* (2006) predict respective opening distances of 192.0 km and 191.3 km, ∼20 per cent greater than and far outside the uncertainty of our estimate.

Differences this large must result from a difference in our respective identifications of C5n.2. In support of this conclusion, Patriat *et al.* (2008) suggest that the magnetic anomaly identified as Anomaly 5 by *Lemaux et al.* (2002) at locations north of the SWIR and west of the Andrew Bain transform fault are instead Anomaly 5B. Based on our own interpretation of the C1n-to-C6no sequence of magnetic anomalies in this region, we concur with Patriat *et al.* (2008). Royer *et al.* (2006) subsequently use the C5n.2 identifications interpreted by Lemaux *et al.* (2002). By implication, the C5n.2 rotations that were estimated in both studies significantly overstate how much new seafloor has been created since 11.06 Ma. In Section 6, we describe the implications of this difference for estimates of rifting in eastern Africa over the past 11 Ma.

Previously published Nubia–Antarctic angular velocities that describe motion during the past 3 Myr (Horner-Johnson *et al.* 2007; DeMets *et al.* 2010) predict seafloor spreading rates that are 15–20 per cent faster than are predicted by our new rotations for Chrons 2An.1 and 2An.3 (Fig. 20A). These differences are mostly at-

tributable to the different corrections for outward displacement that are applied in the three studies. Whereas we correct our rotations for 5 km of outward displacement, as documented in Section 4.1, Horner-Johnson *et al.* (2007) do not adjust their rate estimates for outward displacement and DeMets *et al.* (2010) adjust their rate estimates for a globally averaged 2 km of outward displacement.

5.3.2 Lwandle–Antarctica

Our comparison of Lwandle–Antarctic plate motion to previous estimates is limited to Anomaly 2A, which is the only reversal reconstructed in previous studies (Horner-Johnson *et al.* 2007; DeMets *et al.* 2010). Both of the previously published poles for C2A are located ∼11 angular degrees southeast of our newly estimated poles (Fig. 13A), but are consistent with our new estimates within their large uncertainties. Encouragingly, the velocities predicted by our noise-reduced interval rotations for the past 3 Myr (Supporting Information Table S5) and by the MORVEL Lwandle–Antarctic angular velocity agree to within 1 mm yr^{-1} (Fig. 22A) and ±1° (Fig. 22B). The MORVEL angular velocity is calibrated for 2 km of outward displacement, as is also the case for all of our Lwandle–Antarctic rotations. The ∼1 mm yr^{-1} difference between the spreading rates that are predicted by the Horner-Johnson *et al.* (2007) angular velocity and our rotations (Fig. 22A) is attributable to the absence of any calibration for outward displacement by Horner-Johnson *et al.*

5.3.3 Somalia–Antarctica: C6no, C5n.2 and C2A

Somalia–Antarctic rotations have been estimated most recently for C6no (Patriat *et al.* 2008), C5n.2 (Lemaux *et al.* 2002) and C2A (Horner-Johnson *et al.* 2007; DeMets *et al.* 2010). When corrected for 2 km of outward displacement, the C6no rotation of Patriat *et al.* (2008) predicts total opening of 273.3 km near the midpoint of the Somalia–Antarctic plate boundary (28°S, 65°E). For comparison, our noise-reduced C6no rotation predicts opening of 274.9 ± 2.6 km at the same location. Our respective identifications of C6no along the eastern third of the SWIR are thus highly consistent. The modest difference between our new C6no pole location and that estimated by Patriat *et al.* (2008), as shown in Fig. 16(A), is most likely because our rotation is constrained by fracture zone crossings and by numerous anomaly identifications from the RV *Marion Dufresne* 135 cruise (Cannat *et al.* 2006), which were not available to Patriat *et al.*

The C5n.2 Somalia–Antarctica finite rotation estimated by Lemaux *et al.* (2002) from 152 crossings of C5n.2 east of the Bain fracture zone predicts total opening of 148.4 km near the boundary midpoint (adjusted for 2 km of outward displacement). This differs by less than 1 per cent from the 147.6 ± 2.8 km opening distance predicted by our noise-reduced C5n.2 finite rotation (Supporting Information Table S5). We conclude that our respective identifications of C5n.2 along the Somalia–Antarctic plate boundary are consistent. Despite this good agreement, the Lemaux *et al.* rotation pole falls outside the 95 per cent confidence limits of our new pole (Fig. 16A). We suspect that the difference in pole locations is caused by the additional constraints that are imposed on our rotation by the dense RV *Marion Dufresne* 135 data (Cannat *et al.* 2006) and by fracture zone crossings east of ∼52°E.

The largest differences between our new and previously published estimates of Somalia–Antarctic motion are for the youngest reconstructions, which span the past 3 Myr. The 3-Myr-average
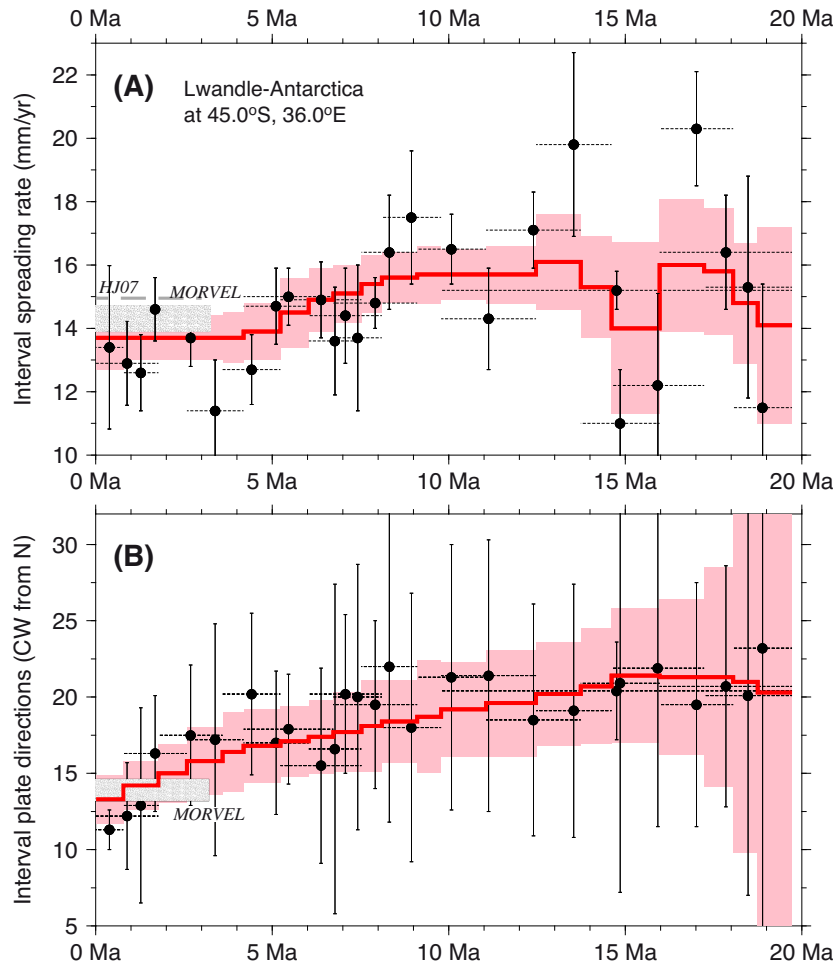
Figure 22. Lwandle–Antarctic plate interval velocities at 45.0°S, 36.0°E. Black circles show interval rates and directions determined from stage rotations that we derived from the best-fitting finite rotations in Table 3. These average plate motion over 1-Myr-long to 3-Myr-long intervals, as indicated by the horizontal dashed lines that are centred on the circles. The red line and pink-shaded area show interval velocities and nominal 1-σ uncertainties determined with the noise-reduced stage rotations from Supporting Information Table S5. (A) Interval seafloor spreading rates. Grey bar is centred on the 3-Myr-average MORVEL Lwandle–Antarctica estimate and encompasses its 1-σ uncertainty. The interval rates use magnetic reversal age estimates from Table 1. 'HJ07' identifies the 3-Ma-average rate predicted by the Lwandle–Antarctic angular velocity of Horner-Johnson *et al.* (2007). (B) Lwandle–Antarctica interval directions. Grey bar shows the MORVEL estimate and encompasses its 1-σ directional uncertainty.

Somalia–Antarctic poles estimated by Horner-Johnson *et al.* (2007) and DeMets *et al.* (2010) are both located far outside of the 95 per cent confidence region for our new best-fitting pole for C2An.3 and are located even farther from the noise-reduced pole (Fig. 16A). We attribute this difference to two factors. The most important factor is the geographic extent of the Somalia–Antarctic data that are used to estimate the rotation. Whereas our rotations are estimated from SWIR data located as far east as the Gallieni transform fault at 52°E, the earlier estimates were estimated only from data between the Atlantis II transform fault at 57°E and the Rodriguez triple junction. As an experiment, we re-estimated a Somalia–Antarctica angular velocity from the MORVEL data, but used all of the MORVEL data between the Gallieni transform fault and the Rodriguez triple junction for the estimate. The resulting Somalia–Antarctic pole moved significantly eastward to the periphery of the 95 per cent confidence region for our new C2An.3 estimate. The pole location is thus sensitive to the geographic distribution of the observations that are used to estimate the pole. A second factor responsible for the difference between our new C2A

estimates and previous estimates is that the recently available, dense magnetic data from the RV *Marion Dufresne* 135 cruise (Cannat *et al.* 2006) impose useful new constraints on the opening rate and opening-rate gradient between 60.5°E and 67°E.

6 IMPLICATIONS AND UNCERTAINTIES

6.1 Southwest Indian Ridge

The newly discovered, simultaneous changes in Nubia–Antarctic, Lwandle–Antarctic and Somalia–Antarctic plate motions at $7.2^{+0.9}_{-1.4}$ Ma may be evidence that the relative motions of the Nubia, Lwandle and Somalia component plates are strongly coupled across their diffuse oceanic boundaries and continental boundaries within the larger Africa plate. Similar evidence has been reported for simultaneous changes in the relative motions within the Capricorn–
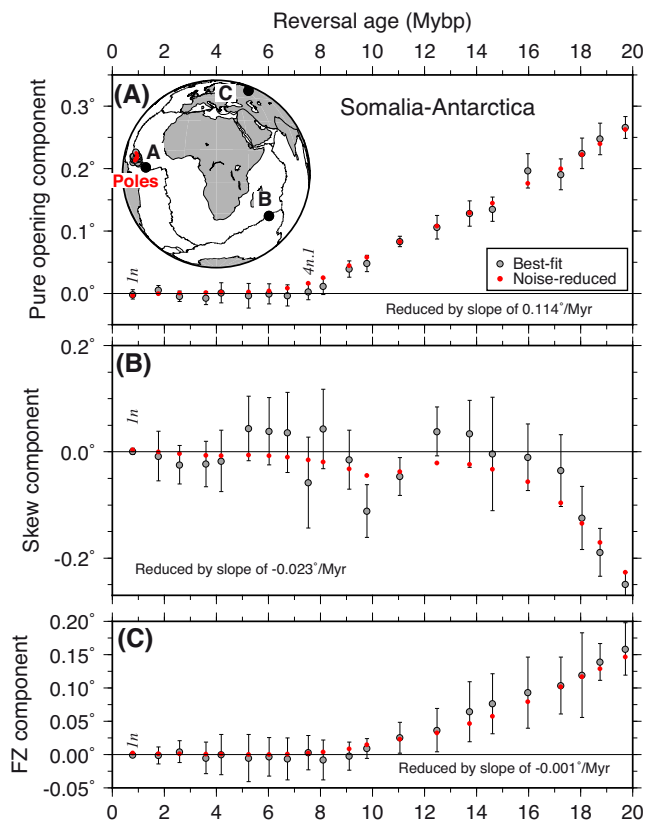
Figure 23. Projections of the Somalia–Antarctica best-fitting (Table 4) and noise-reduced rotations (Supporting Information Table S3) onto Axes A, B and C depicted on the inset globe. Each set of component angles is reduced by the slope that optimizes the fit to the best-fitting component angles for C1n to C4n.1. The slopes defined by the rotation components A and C both change significantly at least once since 20 Ma, consistent with a slowdown in seafloor spreading rates everywhere along the plate boundary and change in the plate slip direction. Uncertainties are 1-σ.

Somalia–India three-plate system (DeMets *et al.* 2005) and the Eurasia–North America–Nubia three-plate circuit (Merkouriev & DeMets 2008; Merkouriev & DeMets 2014a,b). All of these multi-plate circuits include at least one plate pair that is separated entirely or partly by a diffuse oceanic plate boundary. The emerging pattern suggests that strong mechanical coupling across diffuse plate boundaries efficiently transfers the forces that resist and drive the plate motions across the boundary, thereby giving rise to highly correlated plate kinematic changes.

Our analysis also reveals for the first time evidence for unexpectedly large (5 km) outward displacement west of the Andrew Bain transform fault. Given the potential importance of this adjustment to global plate reconstructions, further work is needed to test this result. In a related paper, we use our newly estimated rotations and instantaneous plate velocities predicted by continuously operating GPS sites on the Nubia and Antarctic plates to jointly test the evidence for large outward displacement along the Nubia–Antarctic plate boundary and evaluate the steadiness of Nubia–Antarctic plate motion over the past 7.3 Myr (DeMets, Calais, & Merkouriev, 'Reconciling geodetic and geologic estimates of recent plate motion across the Southwest Indian Ridge', in preparation).

6.2 Rifting in eastern Africa

Our new rotation estimates have important implications for our understanding of opening across the East Africa rift system during the past 11 Ma. From reconstructions of Nubia–Antarctic and Somalia–Antarctic plate motion based on identifications of C5n.2 along the SWIR, Lemaux *et al.* (2002) predict that the Nubia plate has moved 24 km toward N12°W relative to Somalia across the northernmost East Africa rift (10°N, 40°) during the past 11 Myr. The opening direction predicted by their rotation is 60°–80° oblique to the opening direction that is estimated from field structural data in this area (Agostini *et al.* 2011), suggesting a significant error in one of the two estimates. At the same location, a Nubia–Somalia rotation estimated by Royer *et al.* (2006) from their updated reconstructions of C5n.2 along the SWIR predicts 129 ± 62 km (95 per cent) of extension toward N68°W since 11.0 Ma. These two previously published plate kinematic estimates differ by 500 per cent.

A Nubia–Somalia rotation determined from our new Nubia–Antarctic and Somalia–Antarctic rotations for C5n.2 predicts 45 ± 4 km (95 per cent uncertainty) of opening oriented N64°W ± 5° at the same location during the past 11.06 Myr. The predicted motion is relatively insensitive to the correction we apply to the Nubia–Antarctica rotation for outward displacement. For example, if we apply a correction of 2 km instead of 5 km while estimating the C5n.2 Nubia–Antarctic rotation, the modified Nubia–Somalia rotation predicts a 48 ± 4 km of extension, only 3 km larger than our preferred result.

Our revised Nubia–Somalia rotation thus predicts ∼70 per cent less extension between Nubia and Somalia since 11.0 Ma than does the Royer *et al.* (2006) rotation. In equatorial regions of the East African rift (0°N, 28°E), our C5n.2 Nubia–Somalia rotation predicts opening of 38 ± 3 km (95 per cent uncertainty) since 11 Ma, a factor-of-three smaller than predicted by the Royer *et al.* (2006) rotation (113 km) and much closer to total opening estimates of ∼15 km that are based on geologic observations (Morley 1988; Ebinger 1989).

We describe in detail new, high-resolution Nubia–Somalia rotations and their implications in a forthcoming publication (DeMets & Merkouriev 'High-resolution estimates of Nubia–Somalia plate motion since 20 Ma from reconstructions of the Southwest Indian Ridge, Red Sea, and Gulf of Aden', in preparation).

6.3 Uncertainties and need for additional data

Estimates of SWIR and global plate kinematics during the Quaternary and Neogene would benefit significantly from improved magnetic and bathymetric coverage of two areas along the ridge, namely, the seafloor just east of the Bouvet triple junction and older seafloor that flanks the 16°–25°E spreading supersegment. In both areas, improved mapping of the magnetic reversals older than C5An.2 and in particular of Chron 6 is critical for improving the reliability of Nubia–Antarctic rotations for times before 11 Ma.

Modern surveys of the central third of the SWIR, where Lwandle–Antarctic plate motion occurs, are also needed, particularly east of the Prince Edward fracture zone. Although numerous tracks from older cruises cross this part of the SWIR, their navigation, orientation and magnetic sampling rates are sub-optimal and limit our ability to define Lwandle–Antarctic plate motion. We consider this a lower priority given the more limited importance of the Lwandle–Antarctic plate pair to global plate reconstructions.
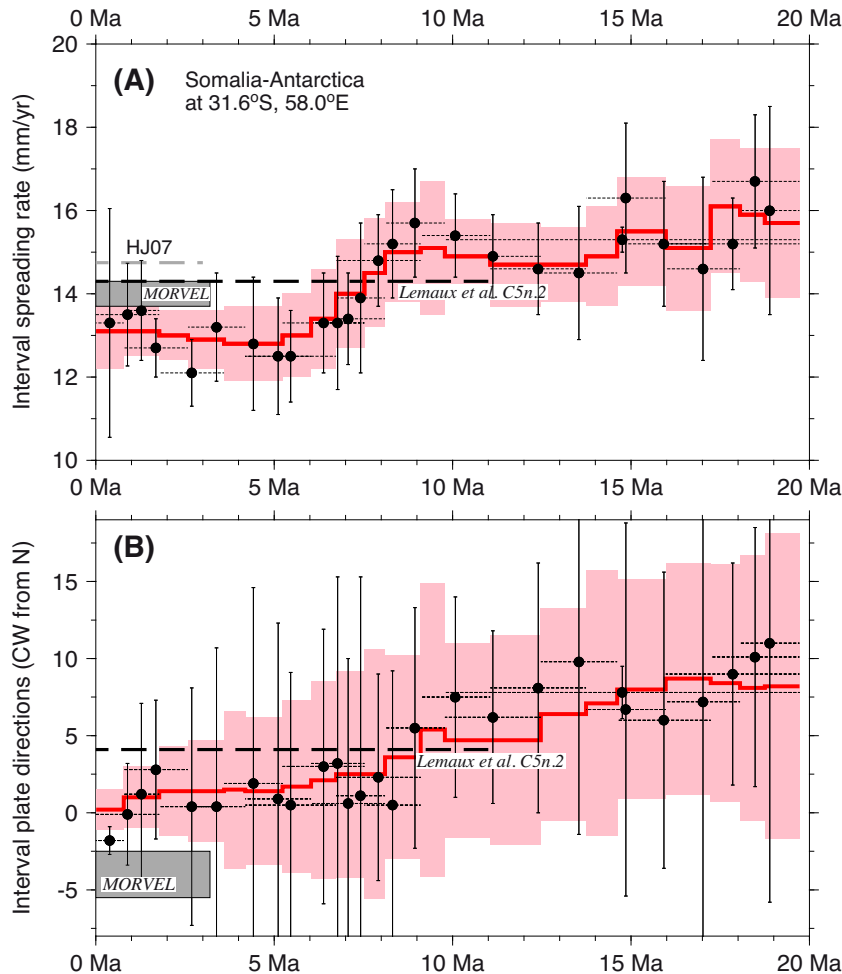
Figure 24. Somalia–Antarctic interval plate velocities at 31.6°S, 58.0°E near the Atlantis II fracture zone. Velocities shown by the circles and their 1-σ uncertainties are determined with stage rotations and covariances derived from the best-fitting finite rotations in Table 4. The red line and pink-shaded area show interval velocities and nominal 1-σ uncertainty estimated with the noise-reduced stage rotations from Supporting Information Table S6. (A) Interval seafloor spreading rates. Grey bar is centred on the 3-Myr-average MORVEL Somalia–Antarctica estimate and encompasses its 1-σ uncertainty. Bold dashed lines show 0-11 Ma-average estimates from the Lemaux *et al.* (2002) C5n.2 rotation. Horizontal dashed lines specify the time interval spanned by a given stage rotation. 'HJ07' identifies the 3-Ma-average rate predicted by the Horner-Johnson *et al.* (2007) Somalia–Antarctic angular velocity. (B) Somalia–Antarctica interval directions. Grey bar shows MORVEL estimate and encompasses its 1-σ directional uncertainty.

7 CONCLUSIONS

From an analysis of nearly 11 000 kinematic data that sample SWIR plate motions from 20 Ma to the present, we conclude the following:

(1) Outward displacement estimated from dense data in 11 areas along the ridge is an unexpectedly large 5 ± 1 km along the Nubia–Antarctica segment of the ridge, but is consistently 2 ± 1 km elsewhere. Adjusted for outward displacement, the SWIR spreading rate pattern differs from that estimated previously, particularly west of 32°E, where spreading rates are ~15 per cent slower than previously estimated.

(2) Inversions of numerous new observations for reversals C1n through C5n.2 to test for the existence of the previously hypothesized Lwandle plate indicate that the plate exists at a confidence level much greater than 99 per cent.

(3) Magnetic reversal, fracture zone and transform fault data for C1n through C5n.2 between the Bouvet triple junction and 50°E are best fit when a Lwandle–Nubia plate boundary is assumed

to intersect the ridge at or near the Bain transform fault (~32–35°E). Data between the Bain transform fault and Rodriguez triple junction give a best, approximate location for a presumably diffuse Lwandle–Somalia plate boundary at the Gallieni transform fault (52°E).

(4) Our newly estimated best-fitting and noise-reduced rotation sequences for the Nubia–Antarctic, Lwandle–Antarctic and Somalia–Antarctic plate pairs reveal a previously unknown change in the motions of all three plate pairs at $7.2^{+0.9}_{-1.4}$ Ma, consisting of a ~20 per cent slowdown in their spreading rates and $5° \pm 2°$ anticlockwise rotation in the plate slip directions. The plate motions for all three plate pairs appear to have remained steady since 7 Ma within the uncertainties.

(5) Our new Nubia–Antarctica rotation for C5n.2 predicts motion since 11.0 Ma that differs by 20 per cent from that determined from other recently published estimates, most likely due to our revised interpretation of the magnetic anomaly pattern along the western third of the SWIR.
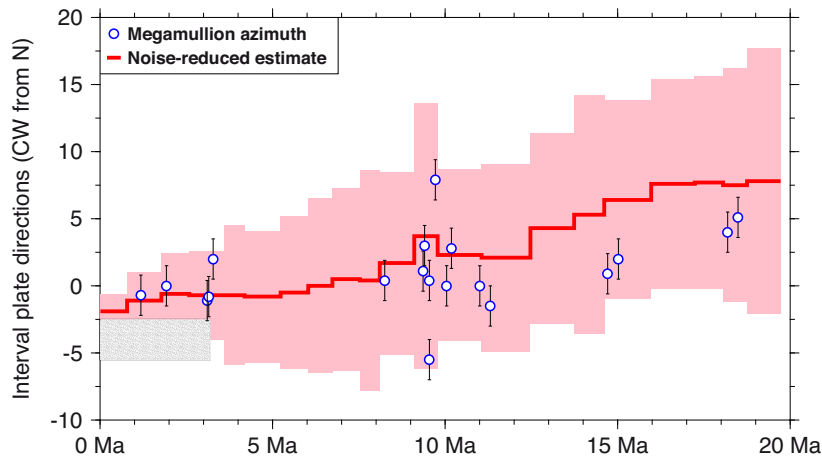
Figure 25. Somalia–Antarctic interval directions at 27.8°S, 64.0°E from stage rotations derived from the noise-reduced rotations in Supporting Information Table S6. The grey bar is centred on the 3-Myr-average MORVEL Somalia–Antarctica estimate and encompasses its 1-σ uncertainty. The mean azimuths of corrugations on axial detachment faults (blue circles) from 62°E and 65°E (Cannat *et al.* 2009) provide independent estimates of interval directions for megamullions that sample different seafloor ages. These typically agree within 0°–2° with the predicted interval directions. An age for each mean corrugation azimuth was estimated by matching its distance from the ridge axis with a flow line reconstructed with Somalia–Antarctic stage rotations.
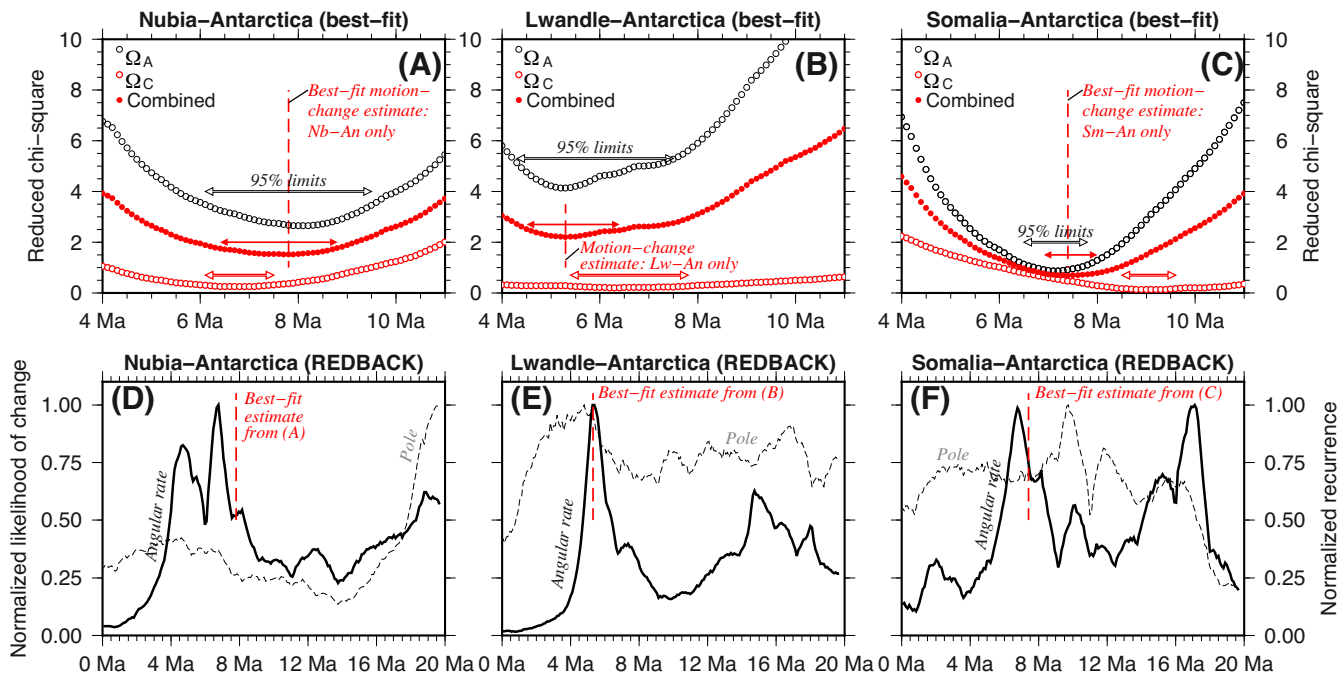

Figure 26. Estimated age of changes in Nubia–Antarctic, Lwandle–Antarctic and Somalia–Antarctic plate motions via two independent approaches. In Panels (A)–(C), the Ω_A and Ω_C components of the best-fitting rotations from Figs 19, 21 and 23 are used to identify possible changes in opening rates and plate slip directions for each plate pair. Assuming that motion since 20 Ma has consisted of two periods of constant motion, separate linear regressions of the component angles that are younger and older than a series of trial change-ages are used to gauge if and when motion changed. Variations in reduced chi-square, the summed least-squares misfit for the two regressions normalized by their summed degrees of freedom, indicate the relative consistency of the component angles with the timing of the assumed change in motion. Panels (D)–(F) show the likelihoods that a change in the angular rotation rate and/or pole location occurred at a given age from a Bayesian analysis of the best-fitting rotation sequence (see the text and Iaffaldano *et al.* 2014). The changes in motion estimated with the two methods agree within 1 Myr.

(6) The newly estimated Nubia–Antarctic and Somalia–Antarctic rotations for C5n.2 predict opening since 11.0 Ma across the East Africa rift that is a factor-of-three less than predicted by the Nubia–Somalia rotation of Royer *et al.* (2006). That the magnitude and direction of the opening predicted by our C5n.2 Nubia–Somalia rotation agree better with geologic estimates than do previous kinematic estimates lend confidence in our newly estimated SWIR plate rotations.
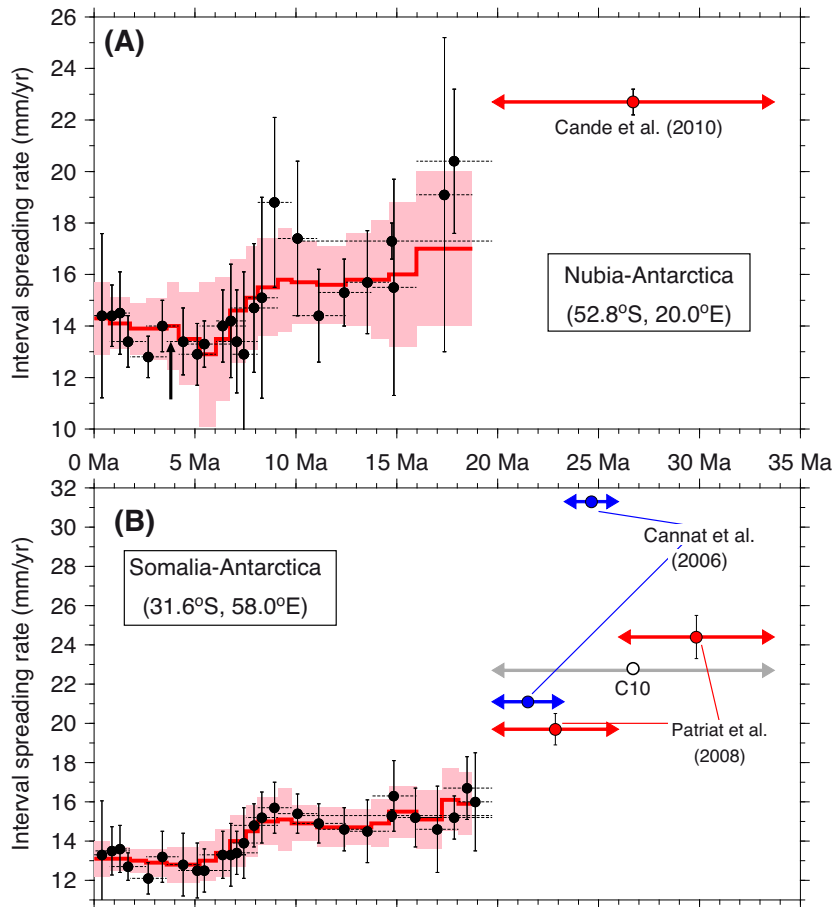
Figure 27. Nubia–Antarctica (A) and Somalia–Antarctica (B) interval spreading rates since 34 Ma near the midpoints of each plate boundary. Red lines and black circles are noise-reduced and best-fitting rates from Figs 20 and 24, respectively. In panel (A), the interval rate labelled 'Cande *et al.* (2010)' is determined from the difference between the C13(old) finite rotation of Cande *et al.* (2010) and the C6no Nubia–Antarctica rotation for this study (Table 2). In panel (B), the interval rates labelled 'Cannat *et al.* (2006)' are determined from C8n.2-to-C6Cn.3 and C6Cn.3-to-C6 stage rotations given in their supplemental material. Interval rates labelled 'Patriat *et al.* (2008)' are estimated from stage rotations we derived from the C13, C8n.2 and C6 finite rotations given in their supplemental material. The rate labelled 'C10' is determined from the difference between the C13(old) finite rotation of Cande *et al.* (2010) and the C6no Somalia–Antarctica rotation for this study (Table 4). All reversal ages are adopted from Ogg (2012).

REFERENCES

Agostini, A., Bonini, M., Corti, G., Sani, F. & Manetti, P., 2011. Distribution of Quaternary deformation in the central main Ethiopian rift, East Africa, *Tectonics,* **30,** TC4010, doi:10.1029/2010TC002833.

Atwater, T. & Mudie, J.D., 1973. Detailed near-bottom geophysical study of the Gorda Rise, *J. geophys. Res.,* **78,** 8665–8686.

Baines, A.G., Cheadle, M.J., Dick, H.J.B., Hosford-Scheirer, A., John, B.E., Kusznir, N.J. & Matsumoto, T., 2007. Evolution of the Southwest Indian Ridge from 55°45′E to 62°E: Changes in plate boundary geometry since 26 Ma, *Geochem. Geophys. Geosyst.,* **8,** Q06022, doi:10.1029/2006GC001559.

Bernard, A., Munschy, M., Rotstein, Y. & Sauter, D., 2005. Refined spreading history at the Southwest Indian Ridge for the last 96 Ma, with the aid of satellite gravity data, *Geophys. J. Int.,* **162,** 765–778.

Cande, S.C., Patriat, P. & Dyment, J., 2010. Motion between the Indian, Antarctic, and African plates in the early Cenozoic, *Geophys. J. Int.,* **183,** 127–149.

Cannat, M., Sauter, D., Mendel, V., Ruellan, E., Okino, K., Escartin, J., Combier, V. & Baala, M., 2006. Modes of seafloor generation at a melt-poor ultraslow-spreading ridge, *Geology,* **34,** 605–608.

Cannat, M., Sauter, D., Escartin, J., Lavier, L. & Picazo, S., 2009. Oceanic corrugated surfaces and the strength of the axial lithosphere at slow spreading ridges, *Earth planet. Sci. Lett.,* **288,** 174–183.

Carbotte, S.M. *et al.*, 2004. New integrated data management system for Ridge2000 and MARGINS research, *EOS, Trans. Am. geophys. Un.,* **85,** 553–559.

Chang, T., 1988. Estimating the relative rotation of two tectonic plates from boundary crossings, *J. Am. Stat. Assoc.,* **83,** 1178–1183.

Chase, C.G., 1972. The *n*-plate problem of plate tectonics, *Geophys. J. R. astr. Soc.,* **29,** 117–122.

Chase, C.G., 1978. Plate kinematics: The Americas, East Africa, and the rest of the world, *Earth planet. Sci. Lett.,* **37,** 355–368.

Chu, D. & Gordon, R.G., 1999. Evidence for motion between Nubia and Somalia along the Southwest Indian Ridge, *Nature,* **398,** 64–67.

DeMets, C. & Wilson, D.S., 2008. Toward a minimum change model for recent plate motions: calibrating seafloor spreading rates for outward displacement, *Geophys. J. Int.,* **174,** 825–841.

DeMets, C., Gordon, R.G., Argus, D.F., Stein, S., DeMets, C., Gordon, R.G. & Vogt, P.R., 1990. Current plate motions, *Geophys. J. Int.,* **101,** 425–478.

DeMets, C., Gordon, R.G. & Royer, J.-Y., 2005. Motion between the Indian, Capricorn, and Somalian plates since 20 Ma: implications for the timing and magnitude of distributed deformation in the equatorial Indian ocean, *Geophys. J. Int.,* **161,** 445–468.

DeMets, C., Gordon, R.G. & Argus, D.F., 2010. Geologically current plate motions, *Geophys. J. Int.,* **181,** 1–80.

Dick, H.J.B. *et al.*, 1991. Tectonic evolution of the Atlantis II Fracture Zone, in *Proceedings of the Ocean Drilling Program, Scientific Results,* Vol. 118, pp. 359–398, eds Von Herzen, R.P. *et al.*, College Station, TX.

Dick, H.J.B., Lin, J. & Schouten, H., 2003. An ultraslow-spreading class of ocean ridge, *Nature,* **426,** 405–412.

Ebinger, C.J., 1989. Tectonic development of the western branch of the East African rift system, *Bull. geol. Soc. Am.,* **101,** 885–903.

Fisher, R.L. & Sclater, J.G., 1983. Tectonic evolution of the Southwest Indian Ocean since the Mid-Cretaceous: plate motions and stability of the pole of Antarctica/Africa for at least 80 Myr, *Geophys. J. R. astr. Soc.,* **73,** 553–576.

Grindlay, N.R., Madsen, J.A., Rommevaux-Jestin, C. & Sclater, J., 1998. A different pattern of ridge segmentation and mantle Bouguer gravity anomalies along the ultra-slow spreading Southwest Indian Ridge (15°30′E to 25°E), *Earth planet. Sci. Lett.,* **161,** 243–253.

Hartnady, C.J.H., 2002. Earthquake hazard in Africa: Perspectives on the Nubia–Somalia boundary, *S. African J. Sci.,* **98,** 425–428.

Hilgen, F.J.J., Lourens, L. & A. Van Dam, J., 2012. The Neogene Period, in *The Geologic Time Scale 2012,* eds Gradstein, F.M., Ogg, J.G., Schmitz, M. & Ogg, E G., Elsevier.

Horner-Johnson, B.C., Gordon, R.G., Cowles, S.M. & Argus, D.F., 2005. The angular velocity of Nubia relative to Somalia and the location of the Nubia–Somalia–Antarctica triple junction, *Geophys. J. Int.,* **162,** 221–234.

Horner-Johnson, B.C., Gordon, R.G. & Argus, D.F., 2007. Plate kinematic evidence for the existence of a distinct plate between the Nubian and Somalian plates along the Southwest Indian Ridge, *J. geophys. Res.,* **112,** B05418, doi:10.1029/2006JB004519.

Hosford, A., Tivey, M., Matsumoto, T., Dick, H., Schouten, H. & Kinoshita, H., 2003. Crustal magnization and accretion at the Southwest Indian Ridge near the Atlantis II fracture zone, 0-25 Ma, *J. geophys. Res.,* **108**(B3), 2169, doi:10.1029/2001JB000604.

Iaffaldano, G., Bodin, T. & Sambridge, M., 2012. Reconstructing plate-motion changes in the presence of finite-rotations noise, *Nature Communications,* **3,** 1048, doi:10.1038/ncomms2051.

Iaffaldano, G., Hawkins, R., Bodin, T. & Sambridge, M., 2014. REDBACK: Open-source software for efficient noise-reduction in plate kinematic reconstructions, *Geochem. Geophys. Geosyst.,* **15,** 1663–1670.

Jestin, F., Huchon, P. & Gaulier, J.M., 1994. The Somalia plate and the East African Rift System: present-day kinematics, *Geophys. J. Int.,* **116,** 637–654.

Kidd, R.G.W., 1977. A model for the process of formation of the upper oceanic crust, *Geophys. J. R. astr. Soc.,* **50,** 149–183.

Kirkwood, B.H., Royer, J.-Y., Chang, T.C. & Gordon, R.G., 1999. Statistical tools for estimating and combining finite rotations and their uncertainties, *Geophys. J. Int.,* **137,** 408–428.

Kumar, R.V. & Gordon, R.G., 2009. Horizontal thermal contraction of oceanic lithosphere: The ultimate limit to the rigid plate approximation, *J. geophys. Res.,* **114,** B01403, doi:10.1029/2007JB005473.

Lawver, L.A. & Scotese, C.R., 1987. A revised reconstruction of Gondwana, in *Gondwana Six: Structure, Tectonics, and Geophysics,* ed. McKenzie, G.D., American Geophysical Union.

Lemaux, J., Gordon, R.G. & Royer, J.-Y., 2002. Location of the Nubia–Somalia boundary along the Southwest Indian Ridge, *Geology,* **30,** 339–342.

Ligi, M. *et al.*, 1999. Bouvet triple junction in the South Atlantic: Geology and evolution, *J. geophys. Res.,* **104,** 29 365–29 386.

Lourens, L., Hilgen, F.J., Laskar, J., Shackleton, N.J. & Wilson, D., 2004. The Neogene Period, *A Geologic Time Scale 2004,* 409–440 Gradstein, F., Ogg, J. & Smith, A., Cambridge Univ. Press.

Macdonald, K.C., Miller, S.P., Luyendyk, B.P., Atwater, T.M. & Shure, L., 1983. Investigation of a Vine-Matthews magnetic lineation from a submersible: the source and character of marine magnetic anomalies, *J. geophys. Res.,* **88,** 3403–3418.

Merkouriev, S. & DeMets, C., 2006. Constraints on Indian plate motion since 20 Ma from dense Russian magnetic data: implications for Indian plate dynamics, *Geochem. Geophys. Geosyst.,* **7,** Q02002, doi:10.1029/2005GC001079.

Merkouriev, S. & DeMets, C., 2008. A high-resolution model for Eurasia-North America plate kinematics since 20 Ma, *Geophys. J. Int.,* **173,** 1064–1083.

Merkouriev, S. & DeMets, C., 2014a. High-resolution estimates of Nubia–North America plate motion: 20 Ma to present, *Geophys. J. Int.,* **196,** 1299–1310.

Merkouriev, S. & DeMets, C., 2014b. High-resolution Quaternary and Neogene reconstructions of Eurasia-North America plate motion, *Geophys. J. Int.,* **198,** 366–384.

Minster, J.B. & Jordan, T.H., 1978. Present-day plate motions, *J. geophys. Res.,* **83,** 5331–5354.

Minster, J.B., Jordan, T.H., Molnar, P. & Haines, E., 1974. Numerical modeling of instantaneous plate tectonics, *Geophys. J. R. Astr. Soc.,* **36,** 541–576.

Molnar, P., Pardo-Casas, F. & Stock, J., 1988. The Cenozoic and Late Cretaceous evolution of the Indian Ocean basin: uncertainties in the reconstructed positions of the Indian, African and Antarctic plates, *Basin Res.,* **1,** 23–40.

Morley, C.K., 1988. Variable extension in Lake Tanganyika, *Tectonics,* **7,** 785–801.

Ogg, J.G., 2012. Geomagnetic polarity time scale, *The Geologic Time Scale 2012,* eds Gradstein, F.M., Ogg, J.G., Schmitz, M. & Ogg, E.G., Elsevier.

Patriat, P., 1983. *Evolution du systeme de dorsale de l'Ocean Indien, These d'Etat,* Universite de Paris.

Patriat, P., Segoufin, J., Goslin, J. & Beuzart, P.1985. Relative positions of Africa and Antarctica in the Upper Cretaceous: Evidence for non-stationary behavior of fracture zones, *Earth planet. Sci. Lett.,* **75,** 204–214.

Patriat, P., Sauter, D., Munschy, M. & Parson, L., 1997. A survey of the Southwest Indian ridge axis between Atlantis II fracture zone and the Indian Ocean triple junction: regional setting and large scale segmentation, *Mar. Geophys. Res.,* **19,** 457–480.

Patriat, P., Sloan, H. & Sauter, D., 2008. From slow to ultraslow: A previously undetected event at the Southwest Indian Ridge at ca. 24 Ma, *Geology,* **36,** 207–210.

Royer, J.-Y. & Chang, T., 1991. Evidence for relative motions between the Indian and Australian plates during the last 20 Myr from plate tectonic reconstructions: implications for the deformation of the Indo-Australian plate, *J. geophys. Res.,* **96,** 11 779–11 802.

Royer, J.Y., Patriat, P., Bergh, H.W. & Scotese, C.R., 1988. Evolution of the Southwest Indian Ridge from the Late Cretaceous (anomaly 34) to the Middle Eocene (anomaly 20), *Tectonophysics,* **155,** 235–260.

Royer, J.-Y., Gordon, R.G. & Horner-Johnson, B.C., 2006. Motion of Nubia relative to Antarctica since 11 Ma: implications for Nubia–Somalia, Pacific-North America, and India-Eurasia motion, *Geology,* **34,** 501–504.

Sandwell, D.T. & Smith, W.H.F., 1997. Marine gravity anomaly from Geosat and ERS 1 altimetry, *J. geophys. Res.,* **102,** 10 039–10 054.

Sauter, D. *et al.*, 2001. The Southwest Indian Ridge between 49°15′E and 57°E: focused accretion and magma redistribution, *Earth planet. Sci. Lett.,* **192,** 303–317.

Sauter, D., Cannat, M. & Mendel, V., 2008. Magnetization of 0-26.5 Ma seafloor at the ultraslow spreading Southwest Indian Ridge, 61°–67°E, *Geochem. Geophys. Geosyst.,* **9,** Q04023, doi:10.1029/2007GC001764.

Schouten, H. & Denham, C.R., 1979. Modeling the oceanic magnetic source layer, in *Deep Drilling Results in the Atlantic Ocean: Ocean Crust,* Maurice Ewing Series, Vol. 2, pp. 151–159, eds Talwani, M., Harrison, C.G. & Hayes, D.E., American Geophysical Union.

Sclater, J.G., Grindlay, N.R., Madsen, J.A. & Rommevaux-Jestin, C., 2005. Tectonic interpretation of the Andrew Bain transform fault, southwest Indian Ocean, *Geochem. Geophys. Geosyst.,* **6,** Q09K10, doi:10.1029/2005GC000951.

Sempere, J.-C., Macdonald, K.C. & Miller, S.P., 1987. Detailed study of the Brunhes/Matuyama reversal boundary on the East Pacific Rise at 19°30′S: implications for crustal emplacement processes at an ultrafast spreading center, *Mar. geophys. Res.,* **9,** 1–23.

Stamps, D.S., Calais, E., Saria, E., Hartnady, C., Nocquet, J.-M., Ebinger, C.J. & Fernandes, R.M., 2008. A kinematic model for the East African Rift, *Geophy. Res. Lett.,* **35,** L05304, doi:10.1029/2007GL032781.

Stein, S. & Gordon, R.G., 1984. Statistical tests of additional plate boundaries from plate motion inversions, *Earth planet. Sci. Lett.,* **69,** 401–412.

Wessel, P. & Smith, W.H.F., 1991. Free software helps map and display data, *EOS, Trans. Am. geophys. Un.,* **72,** 441–446.

Wilson, D.S., 1993. Confidence intervals for motion and deformation of the Juan de Fuca plate, *J. geophys. Res.,* **98,** 16 053–16 071.

SUPPORTING INFORMATION

Additional Supporting Information may be found in the online version of this paper:

(http://gji.oxfordjournals.org/lookup/suppl/doi:10.1093/gji/ggv366/-/DC1).

Please note: Oxford University Press is not responsible for the content or functionality of any supporting materials supplied by the authors. Any queries (other than missing material) should be directed to the corresponding author for the paper.